Microscopic Machine Vision Based Degradation Monitoring of Low-Voltage Electromagnetic Coil Insulation Using Ensemble Learning in a Membrane Computing Framework

CHEN LI[1], FANJIE KONG[1,2], KAI WANG[3], AIDONG XU[3], GEXIANG ZHANG[4], NING XU[5], ZHIHUA LIU[3], HAIFENG GUO[3], XUE WANG[1], KUAN LIANG[1], JIANYING YUAN[4,6], SHOULIANG QI[1], AND TAO JIANG[6]

[1]Microscopic Image and Medical Image Analysis Group, MBIE College, Northeastern University, Shenyang 110819, China
[2]Pratt School of Engineering, Duke University, Durham, NC 27708, USA
[3]Shenyang Institute of Automation, Chinese Academy of Sciences, Shenyang 110016, China
[4]School of Electrical Engineering, Southwest Jiaotong University, Chengdu 611756, China
[5]School of Art and Design, Liaoning Shihua University, Fushun 113001, China
[6]Control Engineering College, Chengdu University of Information Technology, Chengdu 610103, China

Corresponding author: Kai Wang (wangkai@sia.cn) and Tao Jiang (jiang@cuit.edu.cn)

ABSTRACT In this paper, a novel microscopic machine vision system is proposed to solve a degradation monitoring problem of low-voltage electromagnetic coil insulation in practical industrial fields, where an ensemble learning approach in a compound membrane computing framework is newly introduced. This membrane computing framework is constituted by eight layers, 29 membranes, 72 objects, and 35 rules. In this framework, multiple machine learning methods, including classical pattern recognition methods and novel deep learning methods, are tested and compared. First, the most optimal feature extraction approaches are selected. Then, the selected approaches are fused together to achieve an even better monitoring performance. Third, a large number of experiments are used to evaluate and prove the usefulness and potential of the proposed system, where a mean accuracy of 61.4% is achieved on 1035 validation images of six degradation states with single state matching, and mean accuracies of 61.0% and 77.4% are achieved on 622 test images of six degradation states with single state matching and state range matching, respectively. Finally, a mechanical device is designed to apply the system to real industrial tasks.

INDEX TERMS Low-voltage electromagnetic coil, insulation degradation monitoring, ensemble learning, machine vision, membrane computing, microscopic image analysis, feature extraction.

I. INTRODUCTION

Electromagnetic coils are fundamental energy conversion and transformation components of many systems, and they are widely used in motors, transformers, and solenoids [1]. With the increasing use of electric power in aircraft, the reliability of the low-voltage coil insulation systems becomes a very important issue. Many existing works, particularly [2]–[5], report that stator-winding insulation is one of the weakest components in a drive, which contributes to around

25% to 40% of motor failures. A study conducted by 'Oak Ridge National Laboratory' [6] shows that over 50% of solenoid valve failures (SOVs) in U.S. nuclear power plants are attributed to electromagnetic coil faults (such as coil open or coil short). 'CIGRE Study Committee' carries out an international survey, which shows that 56% of electric generator failures are originated by electrical insulation damage [7], [8]. Considering that insulation failure usually occurs suddenly and causes catastrophic effects (for example, it only takes less than 2 seconds for a turn-to-turn fault to develop into a completely winding insulation failure for a 15 KW induction machine), methods to perform degradation monitoring for

The associate editor coordinating the review of this manuscript and approving it for publication was Habib Ullah.

coil insulation are preferred to enable predictive maintenance of the electromagnetic coils prior to development of a fault that could cause catastrophic damage.

In order to solve the degradation monitoring problem mentioned above, a novel *Machine Vision* based intelligent system is proposed in this paper, which can monitor the degradation of low-voltage electromagnetic coil insulation in a rapid and non-destructive way by directly analyzing microscopic images. An example of the analyzed electromagnetic coil and its microscopic images is shown in FIGURE 1.

This system considers the degradation monitoring work as a material state matching task and address the following three problems:

- The first is a classical pattern recognition methods based overall state matching problem. To effectively match the material states, prior knowledge from the practical domain is an important factor, where the classical pattern recognition methods support an effective way to obtain useful information to describe the properties and characteristics of the material states. In this paper, classical pattern recognition approaches are used step by step, such as image denoising, normalization, color feature extraction, texture feature extraction, feature selection and feature fusion [9], [10]. Because in the classical pattern recognition methods, most of the feature extraction approaches are designed manually, they gain an impressive overall state matching result. Based on lots of contrast tests, color features in the RGB color space and *Histogram of Orientation Gradient* (HOG) features obtain the first two overall state matching results among ten classical feature extraction methods (Sec. III-C1). Hence, RGB color features and HOG features are selected for a further fusion.

- The second is a novel *Deep Learning* (DL) methods based single state matching problem. Although, the classical pattern recognition methods can obtain a good overall matching result, they are mainly manual craft methods which are limited by the human imagination and experiences, and easy to ignore the relations among details of information. To this end, novel deep learning approaches introduce a more free way to discover deeper features by machine itself [11]. Although the deep learning methods are lack of prior knowledge from the practical work, they can analyze data using a layer-by-layer learning process, and have a powerful discriminative ability within the inner relations among the data. Hence, besides the classical pattern recognition methods, the deep learning methods are also chosen to further enhance the matching performance in each of the single state. Particularly, this paper focuses on a *Deep Convolutional Neural Network* (DCNN) method, due to its highly evaluated performance in a vast number of machine vision tasks, including image processing, segmentation, classification, video captioning, object detection, tracking and action recognition [12]. However, even the degradation monitoring experiments
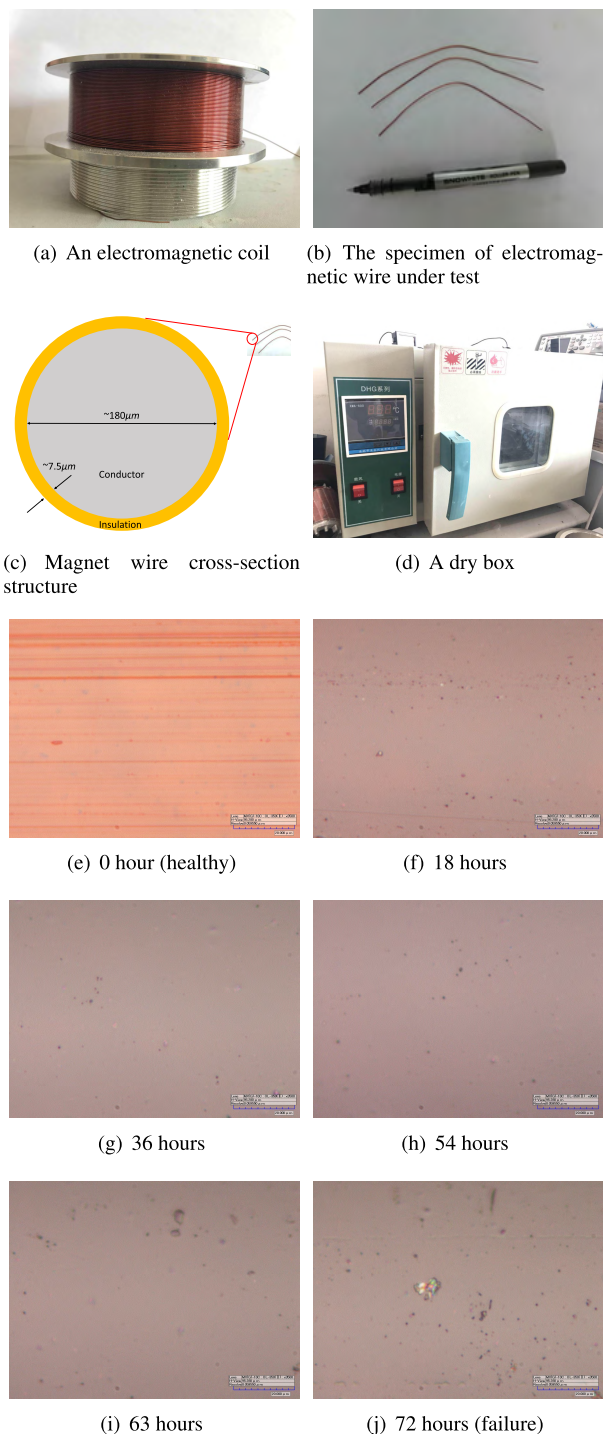

(a) An electromagnetic coil

(b) The specimen of electromagnetic wire under test

(c) Magnet wire cross-section structure

(d) A dry box

(e) 0 hour (healthy)

(f) 18 hours

(g) 36 hours

(h) 54 hours

(i) 63 hours

(j) 72 hours (failure)

FIGURE 1. An example for different degradation cycles (states) of low-voltage electromagnetic coil insulation. (a) to (c) show the visible morphology and structure of the coil and its wire. (d) shows a constant-temperature dry box, where the coil are treated by a 235°C temperature to speed up the degradation process using it. (e) to (j) are the images taken under a 3500 magnification times microscopy in six degradation states, respectively.

are always operated in manual simulated environments to shorten the experimental period, it still takes a very long time to collect the samples, resulting in a small
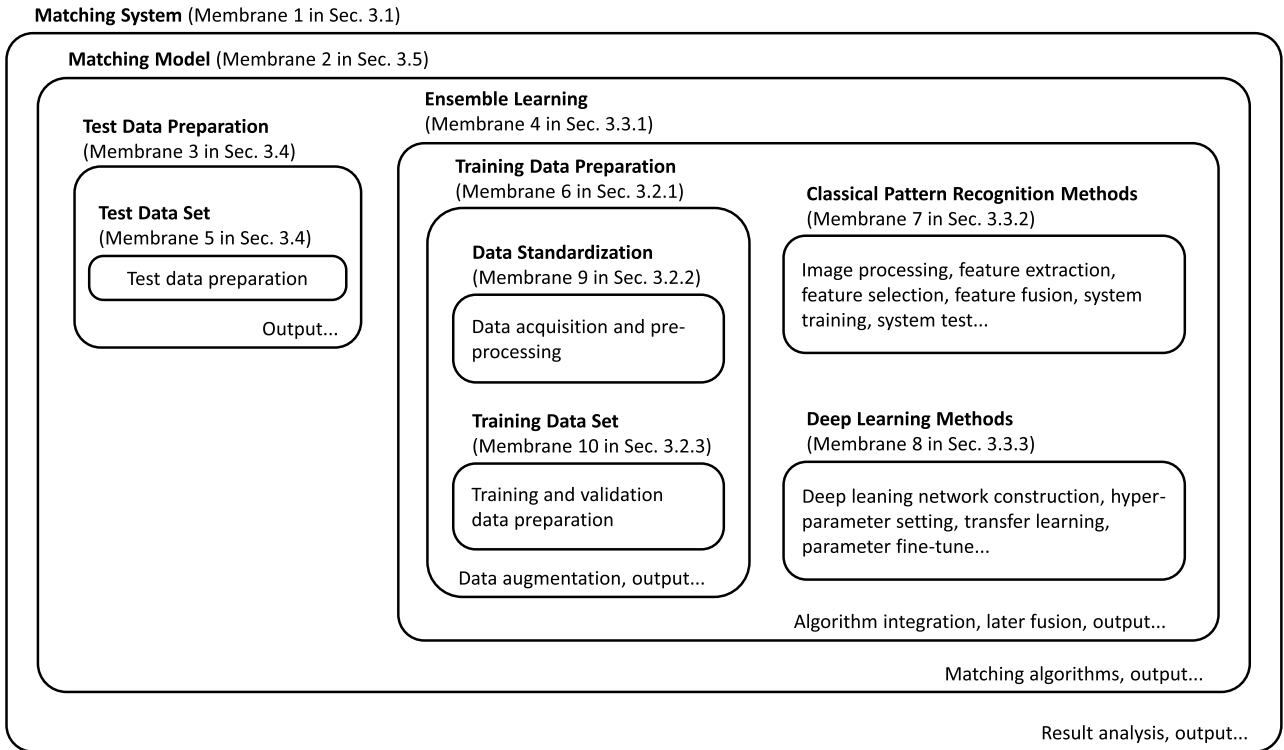
FIGURE 2. A schematic diagram illustrating of the compound cell-like P system of membrane 1.

training data set problem [13]. This problem makes it difficult to collect plenty of microscopic images to train an optimized DCNN model. To this end, data augmentation is first done to increase the size of the data set. Then, a transfer learning strategy is selected and applied by a "pre-training and fine-tuning" approach that first trains a DCNN on a large auxiliary data set, followed by domain-specific fine-tuning on the small microscopic data set [14], [15]. Based on many contrast tests, the DCNN models obtaining the optimal single state matching results are selected for each degradation state, respectively (Sec. III-C2).

- The third is a *Membrane Computing* based *Ensemble Learning* problem. In machine learning domain, because ensemble methods can fuse multiple learning algorithms to obtain a better predictive performance than any of the single learning algorithms [16]–[18], this paper considers to use it to further improve the matching results. In order to apply the ensemble learning strategy effectively, the complementaries of the classical pattern recognition and the novel deep learning based matching methods are first analyzed. Then, based on the analyzing results, a boosting strategy is chosen, which can convert these single "weaker" matching methods into an integrated "stronger" matching method [19], [20]. Especially, because of the good performance of membrane computing systems (P systems) in parallel computing [21], [22], a compound P system framework

is proposed in this paper to integrate the advantages of the weaker matching methods to obtain an even better result. A schematic diagram shown in FIGURE 2 briefly demonstrates the structure of this framework by a Venn diagram [23], where the outermost membrane (skin membrane) is first defined as a cell-like P system to represent the whole matching system (membrane 1 in Sec. III-A). Then, the inside of membrane 1 is constituted by four main P systems: P system for the matching model (membrane 2 in Sec. III-E), P system for test data preparation (membrane 3 in Sec. III-D), P system for ensemble learning (membrane 4 in Sec. III-C), and P system for training data preparation (membrane 6 in Sec. III-B). Furthermore, each of these four P systems is a multi-layer cell-like P system, including the innermost membranes (elementary membranes) inside and conducting the detailed operations on objects and rules of the entire P system. The structure of membrane 1 is briefly represented by Eq. (1) as shown in FIGURE 2.

$$\mu_{\text{brief}} = [\quad [\quad [\quad [\quad]_5]_3 \quad [\quad [\quad [\quad]_9 \\ [\quad]_{10}]_6 \quad [\quad]_7 \quad [\quad]_8]_4]_2]_1. \quad (1)$$

There are three main contributions in this paper:

- First, microscopic machine vision approaches are originally introduced to the practical industrial domain of the degradation monitoring of low-voltage electromagnetic coil insulation.

- Second, a compound membrane computing framework is creatively proposed to solve the ensemble learning problem.
- Thirdly, based on the classical pattern recognition and novel deep learning methods, the ensemble leaning approach achieves successful outcomes.

This paper is structured as follows: Sec. II introduces related works about this paper, Sec. III proposes the detailed methodologies, Sec. IV carries out the experimental results and analysis to attest the effectiveness of the proposed method, Sec. V designs related hardware to apply the proposed methods in practical domains, and finally, Sec. VI closes this paper with a conclusion and future work.

II. RELATED WORK

In this section, related works about this paper are briefly reviewed from six respects: The applications of degradation monitoring in practical industrial fields (Sec. II-A), the usages of microscopic machine vision (Sec. II-B), the development of membrane computing (Sec. II-C), the techniques of ensemble learning (Sec. II-D), the methods of classical pattern recognition (Sec. II-E) and approaches of novel deep learning (Sec. II-F).

A. DEGRADATION MONITORING OF LOW-VOLTAGE ELECTROMAGNETIC COIL INSULATION

Some previous studies address coil insulation degradation monitoring in electrical machinery. The work in [24] performs an accelerated ageing test on twisted pairs of magnet wire and finds that the insulation capacitance increases as breakdown voltage decreases. The phase shift between a signal injects at the coil resonant frequency and the resulting magnetic field is used as a health indicator for the insulation. The work in [25], [26] show that changes in the turn insulation capacitance of the electromagnetic coil are reflected in the resonant frequency. Thus, a monitoring system is developed to detect slight variations of high-frequency resonances in the winding of a working machine fed by an industrial inverter. The work in [27], [28] also places twisted pairs under thermal stress and find that the partial discharge inception voltage decreases, which is an indication of insulation degradation, while the turn-to-turn capacitance increases. Thus they claim that the capacitance can be used as an aging indicator of the self-bonding winding insulation. The work in [29]–[31] propose a method for stator insulation defect detection in traction drives machine windings by evaluating the current response after a voltage step excitation, which is based on the fact that parasitic winding capacitances changes as the insulation degrades. The work in [32] introduces a method to monitor changes in the insulation health state by evaluating the machine high-frequency properties. The work in [33] proposes a solenoid-operated valve (SOV) coil insulation health monitoring method based on the impedance spectrum, in which the accelerated degradation test of the SOV coil is performed and Spearman correlation coefficient is used to find frequency regions of interest within the impedance

spectrum. In essence, all the methods mentioned above use high-frequency electrical parameter measurement (such as impedance, capacitance, and resonance) based techniques for insulation degradation monitoring. Therefore, other effective methods, like high-frequency signal generators, machine vision and artificial intelligence approaches, should be developed and integrated into the devices under test and monitoring, which make a wider way for insulation degradation monitoring in practical applications. As far as we know, currently, only our previous work in [34] introduces machine vision based method to this field, where color features in different color spaces are extracted and compared. Based on this work, we further carry out our new attempt in this paper.

B. MICROSCOPIC MACHINE VISION

Machine vision usually denotes the techniques and approaches which are used to support imaging-based automatic inspection and analysis for industrial and scientific applications [35]–[37]. Due to the effectiveness of the machine vision approaches, they are widely used in many microscopic image analysis tasks, such as microbiological analysis [38], cell analysis [39], pathology analysis [40], and material analysis [41]. For example, in [42], machine vision methods are applied to classify environmental microorganisms into 15 categories, where image segmentation, global feature extraction, local feature extraction, feature fusion, classifier design techniques are continuously applied. In [43], a DCNN based feature learning approach is proposed to synchronously segment and classify epithelial and stromal regions in microscopic histopathological images. A cell clustering work is carried out in [44], where human pluripotent stem cells are automatically grouped into different morphological styles to monitor the differentiation process. In the work of [45], a machine vision method is proposed to match the material of transparent objects using the background distortions, where texture features and surrounding information are jointly applied. However, as far as we know, except our previous work in [34], there is no existing work in the microscopic machine vision domain, which focuses on the degradation monitoring tasks. Hence, this paper introduces the microscopic machine vision methods into a brand-new industrial application field.

C. MEMBRANE COMPUTING

Membrane computing, also known as membrane system or P system, is an active and fast developing research domain in natural computation area, focusing on the study of computing models [46]. Membrane computing gains inspiration from the organization of living cells and their biochemical characteristics, properties, reactions and phenomena [47]. Currently, the membrane computing approaches are applied in many industrial and scientific fields, referring to theoretical aspects [48], [49], applications in computer science, computer graphics, natural language analysis [21], as well as systems and synthetic biology research [22]. In [50], the main research topics and developments are further surveyed with

more detailed information. Since 1998 Păun proposed the original idea of membrane computing till now [51], it is applied in many practical fields, such as robot control [52], electric power system fault diagnosis [47], ecological problem analysis [46], and image processing [53]. For example, in the work of [54], a proportional-integral-derivative based P system controller is proposed to solve a dynamic controller problem of wheeled mobile robots, where artificial neural networks and knowledge of experts are applied to tune parameters. In [55], a fuzzy inference based spiking neural P system is designed, which is applied to deal with an electric power system fault diagnosis problem. In [46], probabilistic P systems are used to analyze the breeding and migration of animals, where the populations of giant pandas and scavenger birds are modeled and predicted. In the work of [56], a family of tissue P system is defined to approximate an intensity gradient function of a 2-D image. In [57], a cell-like P system is structured to optimize a multi-level thresholding criterion for an image segmentation task. In [58], a modified membrane-inspired algorithm based on particle swarm optimization with hyperparameter is used to obtain a optimal image thresholding for image segmentation. However, although membrane computing shows very powerful abilities in many application fields, it is not introduced to the ensemble learning domain before this paper, leaving a huge research space with full of potential.

D. ENSEMBLE LEARNING
In machine learning fields, ensemble learning approaches aim to integrate multiple learning algorithms together for obtaining a better predictive result than each of the original single algorithms [16]–[18]. There are different ensemble learning strategies, such as Bayes optimal classifiers [59], Bayesian parameter averaging [60], bootstrap aggregating [61], and boosting [20]. For instance, the Bayes optimal classifier is an ensemble learning method for classification, and it considers all of the hypotheses in the hypothesis space. Hence, it should be the best ensemble learning method from the theoretical point [59]. But, its performance in piratical work is usually limited by the data size and applied statistical approaches. To this end, Bayesian parameter averaging is proposed, which can approximate the conditions of the Bayes optimal classifier by a hypotheses sampling strategy [60]. Bootstrap aggregating (bagging) denotes an ensemble learning strategy that each learning method has an equal weight in an ensemble voting process. In order to obtain the best predictive result, a bagging approach trains each learning method using a randomly drawn subset of the training set, where the famous 'random forest' algorithm is a successful example for the bagging strategy [61]. Boosting represents an incremental ensemble learning process that can enhance the classification result by training and integrate new single learning methods [20]. In practical work, the boosting method shows a very good classification performance. However, to the best of our knowledge, there is no work applying the powerful membrane computing methods in the

ensemble learning tasks. Hence, this paper attempts to structure a membrane computing framework to implement a novel and feasible ensemble learning method.

E. CLASSICAL PATTERN RECOGNITION METHODS
Pattern recognition is an important application field of machine learning, and it concentrates on identification, recognition and classification tasks of different data types [9], [10]. Especially, classical pattern recognition methods usually refer to image processing, feature extraction, data post processing and classifier design techniques in many microscopic machine vision tasks [62]. Because most of the classical pattern recognition methods are manual designed and include a lot prior knowledge summarized from human experiences, they support highly evaluated performance. For example, in the work of [63], a multi-scale conditional random fields based image labeling approach is proposed, in which each pixel is assigned to one of a finite set of labels by its contextual features. In [64], a method for false positive reduction in mammography is introduced, where multi-scale wavelet and gray level co-occurrence matrix (GLCM) features are extracted first, then particle swarm optimization is used for feature selection, finally a support vector machine is applied for classification.

F. DEEP LEARNING METHODS
Deep learning is a category of machine learning algorithms [65], and most of the modern deep learning models are based on artificial neural networks, such as deep recurrent neural networks, deep residual networks, and DCNNs [66]. Especially, because the DCNNs can effectively find the inner relations of the image data, they show very good performance not only in daily life picture analyzing domains, but also in special photo understanding fields, like microscopic images, CT images, ultrasound images, remote sensing images [67]. In contrast to the classical pattern recognition methods, the DCNN method combines image processing, feature extraction, data post processing and classifier design steps into one integral hierarchical model, where many complicated and detailed information can be easily discovered by the deep learning process. For example, in the work of [68], a DCNN approach is introduced to classify different categories of alga, where a network with ten convolutional layers, three fully connected layers and four spatial pooling layers is built up. In [69], a novel DCNN structure is designed in a conditional random field model, leading to a powerful classifier that can do image segmentation and image classification in microorganism images jointly. However, although the DCNN method is effective, it needs a lot of data to train a high quality parameter set, and the training process is always limited by a small data problem [13], [70]. To address this problem, the strategy of transfer learning is used, where a basic DCNN structure is first pre-trained using a large auxiliary dataset as the ImageNet dataset [71], and then this basic structure is modify by a fine-tuning approach using a domain-specific small dataset [14], [15]. For example, in the work of [72],

a transfer learning based algorithm is proposed to identify retinal pathologies using optical coherence tomography, where GoogLeNet is used as the basic DCNN structure for the pre-training process. Due to the impressive performance of DCNN and transfer learning in microscopic machine vision fields, it is selected for the degradation monitoring work in this paper.

G. SUMMARY

In this section, the related works are reviewed from six points, including degradation monitoring of low-voltage electromagnetic coil insulation, microscopic machine vision, membrane computing, ensemble learning, classical pattern recognition, and novel deep learning. By this brief survey, the following cases are found:

- Although degradation monitoring of low-voltage electromagnetic coil insulation is very important for practical industrial production, only traditional physical and electrical methods are used.
- Because microscopic machine vision methods are very effective, a technological opportunity is provided to the degradation monitoring task above.
- Because membrane computing, ensemble learning, classical pattern recognition methods and novel deep learning approaches are effective algorithms, they are selected and further developed for the microscopic machine vision work in this paper.

III. METHODS

In this section, the technical details of the proposed membrane computing framework are illuminated by the following order: In Sec. III-A, the structure, objects, and rules are integrally defined and introduced; in Sec. III-B, III-C, III-D and III-E, the details in the framework are proposed, respectively; in Sec. III-F, the discussions in this section are summarized.

A. THE MATCHING SYSTEM

As an extension of FIGURE 2, the details of the membrane computing framework is shown in FIGURE 3.

This matching system is designed as a compound cell-like P system, namely membrane 1, and it is defined as Eq. (2):

$$\Pi = (\Gamma, \Theta, \mu, \Omega, R, i_o), \qquad (2)$$

where:

- $\Gamma = \{\{X_*\}, \{F_*\}, \{Acc_*\}, \{M_*\}, \{w_*\}, \{y_*\}\}$, is a finite alphabet, denoting the set of objects of the compound P system:

  (1) $\{X_*\} = \{X_0, X_1, \ldots, X_7\}$, is the set of input data (microscopic images). X_0 represents a 3-D matrix including all original images. As shown in FIGURE 4, the horizontal direction denotes the length of the images, the vertical direction represents the width of the images, and the depth direction shows the included images in X_0. In X_0, the images are denoted as $x_{(0,1)}, x_{(0,2)}, \ldots, x_{(0,\kappa)}$, where κ is the number of images.

Similarly, X_1 is a 3-D matrix for standard images, X_2 is for training images, X_3 is for validation images, X_4 is for training images after data augmentation, X_5 is for validation images after data augmentation, X_6 is for test images, and X_7 is for test images after data augmentation. The detailed description of X_0 to X_6 is discussed in Sec. III-B, and X_7 is discussed in Sec. III-D.

(2) $\{F_*\} = \{F_{(S,RGB)}, F_{(V,RGB)}, \ldots, F_{(S,DLB)}\}$, denotes the set of all extracted features of the input images. In this paper, each of the extracted features is represented by a feature vector, and each element in $\{F_*\}$ is a matrix for the feature vectors. Here, the footnote of $\{F_*\}$ is a pair of functional operators like (S, GRB). The first operator has two options, namely 'S' and 'V', where 'S' denotes the standard images in X_1, and 'V' denotes the validation images in X_5. The second operator represents the detailed feature extraction approaches in Sec. III-C, including 'RGB', 'HSV' ..., 'DL' in this paper.

(3) $\{Acc_*\} = \{Acc_{RGB}, Acc_{HSV}, \ldots, Acc_{DL}\}$, represents the set of matching accuracies between the validation images in X_5 and the standard images in X_1. Here, the footnotes 'GRB', 'HSV', ... 'DL' refer to different extracted features of $\{F_*\}$ in Sec. III-C.

(4) $\{M_*\} = \{M_{CPR}, M_{DL}, M_{DLA}, M_{DLB}, M_{DL_1}, \ldots, M_{DL_6}, M_1, \ldots, M_6\}$, denotes the set of all selected matching models. Here, the footnotes 'CPR', 'DL', ..., 'DL$_6$' are related to the models using different feature extraction approaches in Sec. III-C. The footnotes $1, 2, \ldots, 6$ denote the final matching models of six degradation states from 'healthy' to 'failure' as shown in FIGURE 1, respectively.

(5) $\{w_*\} = \{w_1, w_2, \ldots, w_6\}$, is the set of weight combinations of a late fusion approach [73], which is used to integrate the advantages of the selected matching models in $\{M_*\}$, and find the optimal ensemble to enhance the matching ability of the P system (Sec. III-C). Each $\{w_*\}$ is a three dimensional length vector with the format in Eq. (3):

$$\{w_*\} = [w_{(*,1)}, w_{(*,2)}, w_{(*,3)}], \qquad (3)$$

where $w_{(*,1)} + w_{(*,2)} + w_{(*,3)} = 1$, and $0 \leqslant (w_{(*,1)}, w_{(*,2)}, w_{(*,3)}) \leqslant 1$.

(6) $\{y_*\} = \{y_1, y_2, \ldots, y_9\}$, is the set of all test and evaluation results (Sec. III-A and III-E).

- $\Theta = \{1, 2, 3, \ldots, 29\}$, is the set of labels of the membranes, and the detailed information is shown in TABLE 1.

- $\mu = [\ [\ [\ [\ ]_5]_3 \ [\ [\ [\ ]_9 \ [\ [\ ]_{13}$ $[\ ]_{14}]_{10}]_6 \ [\ [\ [\ ]_{15} \ [\ ]_{16} \ [\ ]_{17} \ [\ ]_{18}$ $[\ ]_{19} \ [\ ]_{20} \ [\ ]_{21} \ [\ ]_{22} \ [\ ]_{23} \ [\ ]_{24}]_{11}]_7$ $[\ [\ [\ [\ [\ ]_{28}]_{26} \ [\ [\ ]_{29}]_{27}]_{25}]_{12}]_8]_4]_2]_1$, is demonstrated by an associated tree in FIGURE 5, and it is the extension of μ_{brief} in Eq. (1) in Sec. I, showing the complete form of the membrane structure in FIGURE 3. In μ, there are in total eight layers and 29 membranes, including 16 elementary membranes.
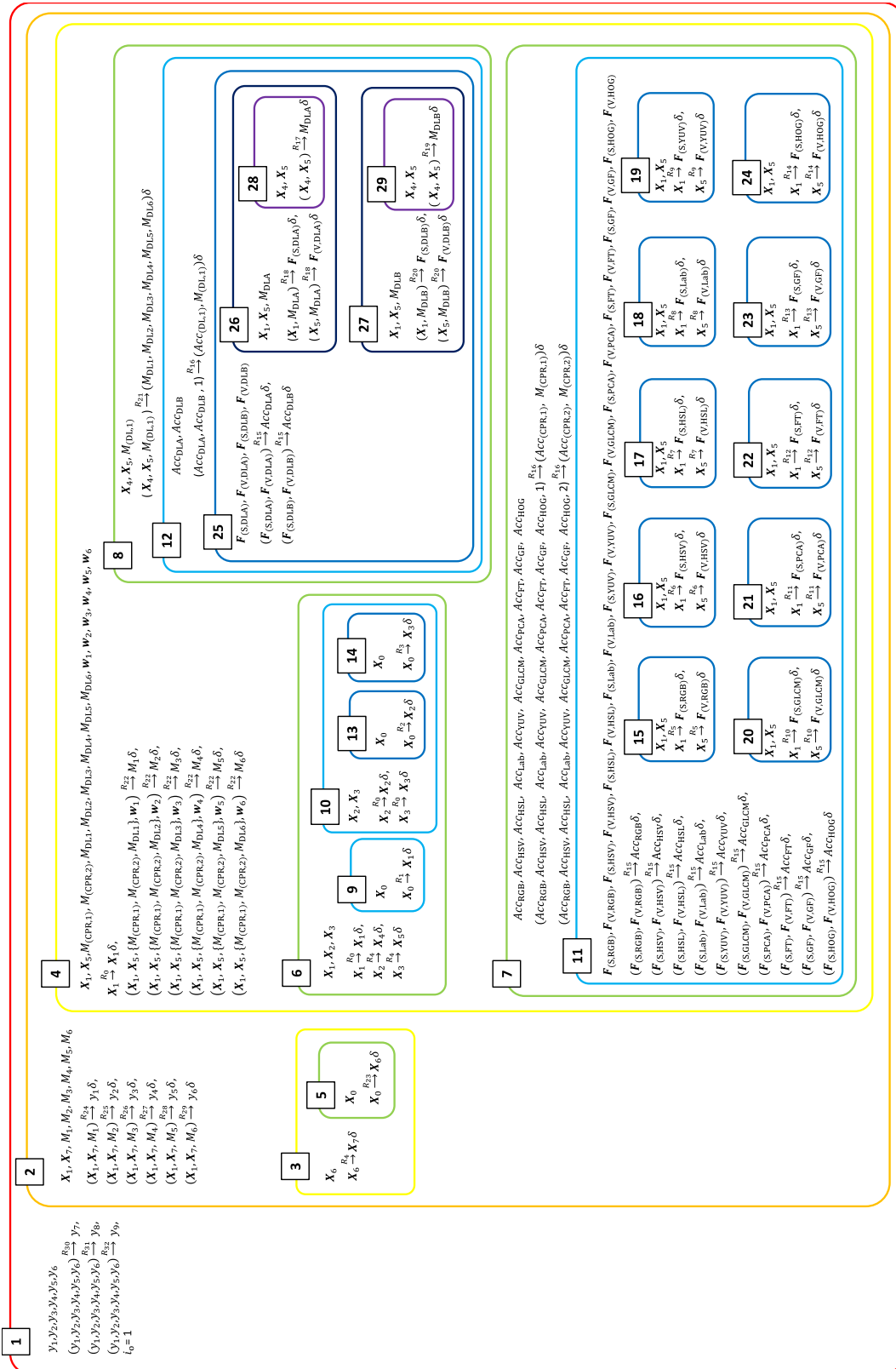
FIGURE 3. The framework of the proposed compound P system. Different colors of the membranes are corresponding to their existing layers, respectively.
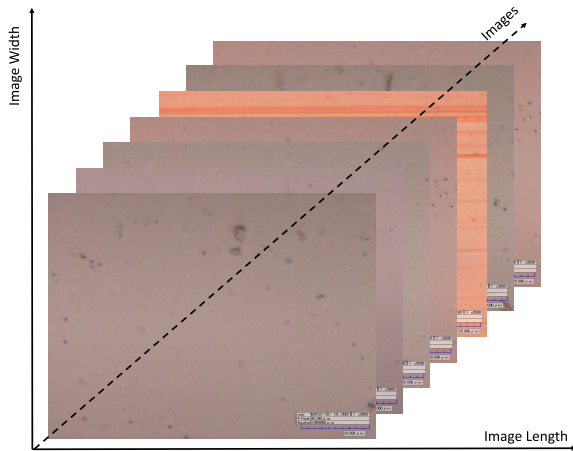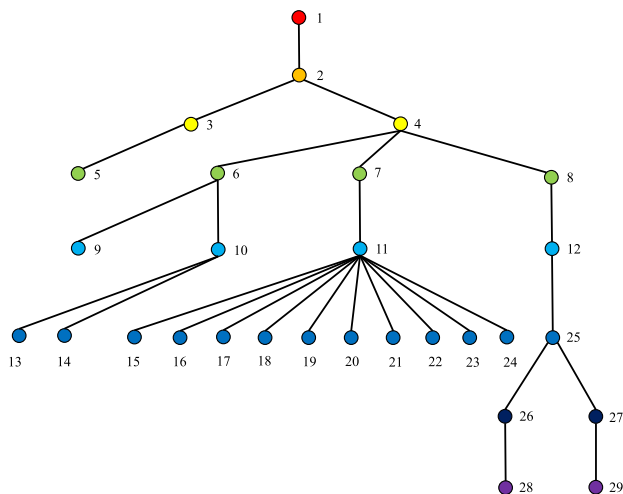
FIGURE 4. An example of the structure of X_0.

FIGURE 5. The associated tree of the membrane structure μ. The colors in different layers are corresponding to the same colors in FIGURE 3, respectively. Membrane 5, 9, 13, 14, 15, 16, 17, 18, 19, 20, 21, 22, 23, 24, 28 and 29 are elementary membranes.

- $\Omega = \{\omega_1, \omega_2, \omega_3, \ldots, \omega_{29}\}$, represents the finite multisets of objects associated with the compartments of μ shown in FIGURE 3 and 5, called 'initial multisets of objects', where:

(1) $\omega_1 = \{y_1, y_2, \ldots, y_6\}$.

(2) $\omega_2 = \{X_1, X_7, M_1, M_2, \ldots, M_6\}$.

(3) $\omega_3 = \{X_6\}$.

(4) $\omega_4 = \{X_1, X_5, M_{(CPR,1)}, M_{(CPR,2)}, M_{DL_1}, \ldots, M_{DL_6}, \{w_*\}\}$.

(5) $\omega_5 = \{X_0\}$.

(6) $\omega_6 = \{X_1, X_2, X_3\}$.

(7) $\omega_7 = \{Acc_{RGB}, Acc_{HSV}, \ldots, Acc_{HOG}\}$.

(8) $\omega_8 = \{X_4, X_5, M_{(DL,1)}\}$.

(9) $\omega_9 = \{X_0\}$.

(10) $\omega_{10} = \{X_2, X_3\}$.

(11) $\omega_{11} = \{F_{(S,RGB)}, F_{(V,RGB)}, \ldots, F_{(V,HOG)}\}$.

(12) $\omega_{12} = \{Acc_{DLA}, Acc_{DLB}\}$.

(13) $\omega_{13} = \{X_0\}$.

(14) $\omega_{14} = \{X_0\}$.

(15) $\omega_{15} = \{X_1, X_5\}$.

(16) $\omega_{16} = \{X_1, X_5\}$.

(17) $\omega_{17} = \{X_1, X_5\}$.

(18) $\omega_{18} = \{X_1, X_5\}$.

(19) $\omega_{19} = \{X_1, X_5\}$.

(20) $\omega_{20} = \{X_1, X_5\}$.

(21) $\omega_{21} = \{X_1, X_5\}$.

(22) $\omega_{22} = \{X_1, X_5\}$.

(23) $\omega_{23} = \{X_1, X_5\}$.

(24) $\omega_{24} = \{X_1, X_5\}$.

(25) $\omega_{25} = \{F_{(S,DLA)}, F_{(V,DLA)}, F_{(S,DLB)}, F_{(V,DLB)}\}$.

(26) $\omega_{26} = \{X_1, X_5, M_{DLA}\}$.

(27) $\omega_{27} = \{X_1, X_5, M_{DLB}\}$.

(28) $\omega_{28} = \{X_4, X_5\}$.

(29) $\omega_{29} = \{X_4, X_5\}$.

- $R = \{R_0, R_1, R_2, \ldots, R_{32}, \delta\}$, denotes the finite sets of multiset rewriting and communication rules associated with the 29 compartments in Ω, where the details of R is shown in TABLE 1.

- $i_o \in \Theta$, defines the output compartment in Θ.

TABLE 1. The labels of the membranes (P systems). The left column shows the labels of each membrane. The right column describes the main function of each membrane.

Label	Main function
1	P system for the matching system
2	P system for the matching model
3	P system for test data preparation
4	P system for ensemble learning
5	P system for test data
6	P system for training data preparation
7	P system for classical pattern recognition methods
8	P system for deep learning methods
9	P system for data standardization
10	P system for training data
11	P system for feature selection of classical pattern recognition methods
12	P system for the second round feature selection of deep learning methods
13	P system for training set
14	P system for validation set
15	P system for red, green, blue (RGB) color space features
16	P system for hue, saturation, value (HSV) color space features
17	P system for hue, saturation, lightness (HSL) color space features
18	P system for luminosity, a, b (Lab) color space features
19	P system for luminosity, chroma (YUV) color space features
20	P system for grey-level co-occurrence matrix (GLCM) features
21	P system for principle component analysis (PCA) features
22	P system for Fourier transform (FT) features
23	P system for Gabor filter (GF) features
24	P system for histogram of orientation gradient (HOG) features
25	P system for the first round feature selection of deep learning methods
26	P system for deep learning method A
27	P system for deep learning method B
28	P system for model training of deep learning method A
29	P system for model training of deep learning method B

B. TRAINING DATA PREPARATION

In this section, the usages and details of membrane 6 (P system for training data preparation) are introduced. Membrane 6 is a cell-like P system as shown in FIGURE 3, and it is used to prepare standard data, training data and validation data. Especially, all the data in this paper are microscopic images as shown in FIGURE 1 (e) to (j).

TABLE 2. Rules in the membrane computing framework. The left column shows the names of the rules. The middle column gives the definitions of the rules. The right column is the descriptions for the rules.

Rule	Definition	Description
R_0	Input $\xrightarrow{R_0}$ Output	Input = Output, to keep the Output the same as the Input.
R_1	Input $\xrightarrow{R_1}$ Output	Input denotes original images and Output represents images after standardization (Sec. III-B1).
R_2	Input $\xrightarrow{R_2}$ Output	Input denotes original images and Output represents training images (Sec. III-B2).
R_3	Input $\xrightarrow{R_3}$ Output	Input denotes original images and Output represents validation images (Sec. III-B2).
R_4	Input $\xrightarrow{R_4}$ Output	Input denotes original images and Output represents images after data augmentation (Sec. III-B3).
R_5	Input $\xrightarrow{R_5}$ Output	Input denotes images and Output represents the extracted 'RGB' feature matrix (Sec. III-C1).
R_6	Input $\xrightarrow{R_6}$ Output	Input denotes images and Output represents extracted 'HSV' feature matrix (Sec. III-C1).
R_7	Input $\xrightarrow{R_7}$ Output	Input denotes images and Output represents the extracted 'HSL' feature matrix (Sec. III-C1).
R_8	Input $\xrightarrow{R_8}$ Output	Input denotes images and Output represents the extracted 'Lab' feature matrix (Sec. III-C1).
R_9	Input $\xrightarrow{R_9}$ Output	Input denotes images and Output represents the extracted 'YUV' feature matrix (Sec. III-C1).
R_{10}	Input $\xrightarrow{R_{10}}$ Output	Input denotes images and Output represents the extracted 'GLCM' feature matrix (Sec. III-C1).
R_{11}	Input $\xrightarrow{R_{11}}$ Output	Input denotes images and Output represents the extracted 'PCA' feature matrix (Sec. III-C1).
R_{12}	Input $\xrightarrow{R_{12}}$ Output	Input denotes images and Output represents the extracted 'FT' feature matrix (Sec. III-C1).
R_{13}	Input $\xrightarrow{R_{13}}$ Output	Input denotes images and Output represents the extracted 'GF' feature matrix (Sec. III-C1).
R_{14}	Input $\xrightarrow{R_{14}}$ Output	where Input denotes images and Output represents the extracted 'HOG' feature matrix (Sec. III-C1).
R_{15}	$(\text{Input}_1, \text{Input}_2) \xrightarrow{R_{15}}$ Output	Input_1 denotes a feature matrix of standard images, Input_2 denotes a feature matrix of validation images (or after data augmentation), and Output represents the matching accuracy between them (Sec. III-C1). In this paper, the matching accuracy is defined as Eq. (4) $$Acc = \frac{\text{Number of Accurately Matched Images}}{\text{Number of All Matched Images}} .\qquad(4)$$ Furthermore, in order to obtain a higher accuracy, multiple classical similarity based matching methods are pre-tested, including Euclidean distance [74], cosine distance [75] and earth mover's distance [76]. Lastly, the Euclidean distance based similarity shows the best performance to match different degradation states, which is defined as Eq. (5). $$S_{(\varepsilon,v)} = 1 - \frac{\sum_{i=1}^{v} |\varepsilon_i - v_i|}{\max(|\varepsilon_i - v_i|) \times v} ,\qquad(5)$$ where ε and v are two v dimensional length vectors, and the similarity $S_{(\varepsilon,v)}$ is a value between $[0,1]$. If $S_{(\varepsilon,v)}$ is the more closer to 1, then v is the more similar to ε.
R_{16}	$(\text{Input}_1, \ldots, \text{Input}_n, \varsigma) \xrightarrow{R_{16}}$ $(\text{Output}_1, \text{Output}_2)$	$n = 1, 2, 3, \ldots$, and $(\text{Input}_1, \ldots, \text{Input}_n)$ are matching accuracies using different feature extraction methods. 1) In an ideal case: If all the features show a distinct difference on the matching accuracies, $\varsigma = 1, \ldots, n$ is an operator to select a method from $\text{Input}_1, \ldots, \text{Input}_n$ by the descending order of accuracies, Output_1 is the selected ςth highest accuracy among them, and Output_2 is the model of the feature extraction method that obtains the Output_1 (Sec. III-C1). 2) In a practical case: If some features obtain high and close matching accuracies to others, the matching variances of them are used as a further measure to compare the stabilities of them. Here, a variance is in $[0,1]$ and the more closer to 0 the more stable. In this case, $\varsigma = 1, \ldots, n$ is an operator to select a method from $\text{Input}_1, \ldots, \text{Input}_n$ by the ascending order of variances, Output_1 is the accuracy according to the selected ςth lowest variance among them, and Output_2 is the model of the feature extraction method that obtains the Output_1 (Sec. III-C1).
R_{17}	$(\text{Input}_1, \text{Input}_2) \xrightarrow{R_{17}}$ Output	Input_1 denotes training images, Input_2 denotes validation images, and Output represents a directly trained deep learning model (Sec. III-C2).
R_{18}	$(\text{Input}_1, \text{Input}_2) \xrightarrow{R_{18}}$ Output	Input_1 denotes images, Input_2 denotes the obtained deep learning model using R_{17} in (18), and Output represents the feature matrix extracted by this deep learning method (Sec. III-C2).
R_{19}	$(\text{Input}_1, \text{Input}_2) \xrightarrow{R_{19}}$ Output	Input_1 denotes training images, Input_2 denotes validation images, and Output represents a pre-trained deep learning model using a transfer learning process (Sec. III-C2).
R_{20}	$(\text{Input}_1, \text{Input}_2) \xrightarrow{R_{20}}$ Output	Input_1 denotes images, Input_2 denotes the obtained deep learning model using R_{19} in (20), and Output represents the feature matrix extracted by this deep learning method (Sec. III-C2).
R_{21}	$(\text{Input}_1, \text{Input}_2, \text{Input}_3) \xrightarrow{R_{21}}$ $(\text{Output}_1, \ldots, \text{Output}_6)$	Input_1 denotes training images, Input_2 represents validation images, Input_3 denotes a selected deep learning model, and $(\text{Output}_1, \ldots, \text{Output}_6)$ represent six further fine tuned deep learning models for six degradation states in this paper, respectively (Sec. III-C2).
R_{22}	$(\text{Input}_1, \ldots, \text{Input}_4) \xrightarrow{R_{22}}$ Output	Input_1 denotes standard images, Input_2 denotes validation images, Input_3 denotes a set of different models for feature extraction methods, and Input_4 represents a set of vectors with fusion weights for the models in Input_3, respectively. The Output denotes a new matching model after the ensemble learning (Sec. III-C3).
R_{23}	Input $\xrightarrow{R_{23}}$ Output	Input denotes original images and Output represents test images (Sec. III-D).
R_{24}	$(\text{Input}_1, \text{Input}_2, \text{Input}_3) \xrightarrow{R_{24}}$ Output	Input_1 denotes standard images, Input_2 shows test images, Input_3 is the matching model for the first degradation state (0 hour, healthy), and Output represents the matching result (Sec. III-E).

TABLE 2. *(Continued.)* Rules in the membrane computing framework. The left column shows the names of the rules. The middle column gives the definitions of the rules. The right column is the descriptions for the rules.

R_{25}	$(\text{Input}_1, \text{Input}_2, \text{Input}_3) \xrightarrow{R_{25}} \text{Output}$	Input_1 denotes standard images, Input_2 shows test images, Input_3 is the matching model for the second degradation state (18 hours), Output represents the matching result (Sec. III-E).
R_{26}	$(\text{Input}_1, \text{Input}_2, \text{Input}_3) \xrightarrow{R_{26}} \text{Output}$	Input_1 denotes standard images, Input_2 shows test images, Input_3 is the matching model for the third degradation state (36 hours), Output represents the matching result (Sec. III-E).
R_{27}	$(\text{Input}_1, \text{Input}_2, \text{Input}_3) \xrightarrow{R_{27}} \text{Output}$	Input_1 denotes standard images, Input_2 shows test images, Input_3 is the matching model for the fourth degradation state (54 hours), Output represents the matching result (Sec. III-E).
R_{28}	$(\text{Input}_1, \text{Input}_2, \text{Input}_3) \xrightarrow{R_{28}} \text{Output}$	Input_1 denotes standard images, Input_2 shows test images, Input_3 is the matching model for the fifth degradation state (63 hours), Output represents the matching result (Sec. III-E).
R_{29}	$(\text{Input}_1, \text{Input}_2, \text{Input}_3) \xrightarrow{R_{29}} \text{Output}$	Input_1 denotes standard images, Input_2 shows test images, Input_3 is the matching model for the sixth degradation state (72 hours, failure), Output represents the matching result (Sec. III-E).
R_{30}	$(\text{Input}_1, \ldots, \text{Input}_6) \xrightarrow{R_{30}} \text{Output}$	$(\text{Input}_1, \ldots, \text{Input}_6)$ denote the matching results of six degradation states, and Output represents the average value of them (Sec. III-A).
R_{31}	$(\text{Input}_1, \ldots, \text{Input}_6) \xrightarrow{R_{31}} \text{Output}$	$(\text{Input}_1, \ldots, \text{Input}_6)$ denote the matching results of six degradation states, and Output represents the variance of them (Sec. III-A).
R_{32}	$(\text{Input}_1, \ldots, \text{Input}_6) \xrightarrow{R_{32}} \text{Output}$	$(\text{Input}_1, \ldots, \text{Input}_6)$ denote the matching results of six degradation states, and Output represents the related values of Gaussian distribution of them [77] (Sec. III-A).
R_{33}	$R_{33} = \{r_2, r_3, r_4, r_6\}$	R_{33} is a set of the initialization rules of the P system, where r_2, r_3, r_4 and r_6 are the initialization rules related to membrane 2, 3, 4, and 6, respectively. Each of these rules has a form as $r_* = (Q_*, S_{(*,0)}, P_*, G_*)$: 1) $Q_* \in \{1,0\}$ is a binary operator of states defined in Eq.eq 6:

$$\text{If } Q_* = \begin{cases} 1, & \text{then the P system works} \\ 0, & \text{then the P system stops} \end{cases}. \tag{6}$$

2) $S_{(*,0)} \in \{1,0\}$ is a binary operator of initial states defined in Eq. (7):

$$\text{If } S_{(*,0)} = \begin{cases} 1, & \text{then the P system is activated} \\ 0, & \text{then the P system is stop} \end{cases}. \tag{7}$$

In this paper, the $S_{(*,0)}$ is set as Eq. (8):

$$\begin{aligned} S_{(2,0)} &= 0 , \\ S_{(3,0)} &= 1 , \\ S_{(4,0)} &= 0 , \\ S_{(6,0)} &= 1 . \end{aligned} \tag{8}$$

3) $P_* \subseteq \Gamma$ is an initial multiset of objects defined in Eq. (9):

$$\begin{aligned} P_2 &= \{X_1, X_7, M_1, M_2, \ldots, M_6\} , \\ P_3 &= \{X_0\} , \\ P_4 &= \{X_1, X_4, X_5\} , \\ P_6 &= \{X_0\} . \end{aligned} \tag{9}$$

4) G_* is a set of rewriting and communication rules for $\{r_2, r_3, r_4, r_6\}$, respectively. In this paper, G_* is represented in a vector format as $G_* = [g_1, g_2, g_3, g_4]$, $g_1 \in \{0,1\}, g_2 \in \{0,1\}, g_3 \in \{0,1\}, g_4 \in \{0,1\}$, $g_2 \neq g_3$, $g_2 \neq g_4$, where:

$$\begin{aligned} &\text{If } g_1 = 1, \text{then do data rewriting ;} \\ &\text{If } g_2 = 1, \text{then do forward data transport ;} \\ &\text{If } g_3 = 1, \text{then do feedback sending ;} \\ &\text{If } g_4 = 1, \text{then do feedback receiving .} \end{aligned} \tag{10}$$

In this paper, G_* is set as follows:

$$\begin{aligned} G_2 &= [1,0,0,0] \text{ or } [0,0,0,0] , \\ G_3 &= [1,1,0,0] \text{ or } [0,0,0,0] , \\ G_4 &= [1,1,0,0] \text{ or } [1,0,1,0] \text{ or } [0,0,0,0] , \\ G_6 &= [1,1,0,0] \text{ or } [1,0,0,1] \text{ or } [0,0,0,0] . \end{aligned} \tag{11}$$

δ	δ	An operator for dissolving a membrane.

Membrane 6 includes one skin membrane and three elementary membranes, and it is represented as Eq. (12):

$$\Pi_6 = (X_*, \{6, 9, 10, 13, 14\}, \mu_6, \{\omega_6 \cup \omega_9 \cup \omega_{10} \cup \omega_{13} \cup \omega_{14}\}, \{R_0, \ldots, R_4, r_6\}), \tag{12}$$

where its structure μ_6 is defined as Eq. (13):

$$\mu_6 = [\ [\ ]_9 \ [\ [\ ]_{13} \ [\ ]_{14}]_{10}]_6. \tag{13}$$

The working process of membrane 6 is shown in Algorithm 1.

Algorithm 1 Workflow of Membrane 6

Input: The original microscopic image set X_0.

Output: The standard image set X_1, the training image set X_4, and the validation image set X_5.

1: Initialize membrane 6, where $S_{(6,0)} = 1$, and $G_6 = [1, 1, 0, 0]$.

2: Run membrane 9, 13 and 14, synchronously.

3: Obtain X_1, X_2, X_3 from membrane 9, 13 and 14, respectively.

4: Dissolve membrane 9, 13, and 14 with δ, and release X_1, X_2, X_3 to their external environments, respectively.

5: Run and dissolve membrane 10, then release X_2, X_3 to their external environments.

6: Run membrane 6.

7: Obtain X_1, X_4, X_5 from membrane 6.

8: Activate membrane 7 and 8 using X_1, X_4, X_5.

9: Update G_6 to [0, 0, 0, 0].

10: **return** X_1, X_4, X_5.

---

1) MEMBRANE 9 (P SYSTEM FOR DATA STANDARDIZATION)

Due to the prior knowledge from the degradation monitoring experts and our previous work, standard images are necessary to represent a general state of the material [34]. To this end, the membrane 9 is designed in this paper, where $X_0 \xrightarrow{R_1} X_1$ is constituted with three steps: First, κ_s original images of each degradation state are randomly selected from X_0, where $2 \leqslant \kappa_s \leqslant (\kappa_{\min} - 1)$ and $\kappa_{\min}$ is the image number of the degradation state with the minimum number samples. Then, a classical image denoising approach, namely median filter [78], is applied to these selected images to reduce the impacts of noise and outlier pixels. Thirdly, in each state, the selected images are summed up and averaged with κ_s. Finally, all the averaged images are used as the standard image set X_1. After the computation above, membrane 9 is dissolved by the rule of δ, and X_1 is released to membrane 6. An example for the image standardization is shown in FIGURE 6.
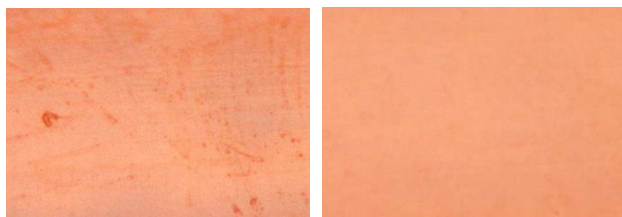
(a) An original image   (b) A standard image

FIGURE 6. An example for the image standardization (at 0 hour).

2) MEMBRANE 10 (P SYSTEM FOR TRAINING DATA)

Because the proposed degradation monitoring system is based on a series of supervised learning approaches, training and validation images are necessary. Hence, membrane 10 (P system for training data) is introduced to generate the training and validation image sets, including two sub-membranes, membrane 13 and 14.

(1) In membrane 13 (P system for training set), the operation of $X_0 \xrightarrow{R_2} X_2$ first works, where p_{Tr} original images of each degradation state are randomly selected from X_0, and $p_{\mathrm{Tr}} \in (0, 1)$ is the sampling rate for training images. Then, these selected images are used as the training image set X_2. Lastly, membrane 13 is dissolved by the rule of δ, and X_2 is released to membrane 10.

(2) In membrane 14 (P system for validation set), the operation of $X_0 \xrightarrow{R_3} X_3$ first works, where p_{V} original images of each degradation state are randomly selected from X_0, and $p_{\mathrm{V}} \in (0, 1)$ is the sampling rate for validation images with the following rules in Eq. (14):

$$
\begin{aligned}
&0 < p_{\mathrm{Tr}} + p_{\mathrm{V}} < 1, \\
&\text{If} \quad x_{(0,i)} \in X_2, \\
&\text{Then} \quad x_{(0,i)} \notin X_3, \quad\quad (14)
\end{aligned}
$$

where $x_{(0,i=1,2,3,\ldots,\kappa)}$, is an image in the X_0 (Sec. III-A). Then, these selected images are used as the validation image set X_3. Lastly, membrane 14 is dissolved by the rule of δ, and X_3 is released to membrane 10.

(3) In membrane 10, the contents of X_2 and X_3 are kept by the rule R_0 first. Then membrane 10 is dissolved by δ, and X_2 and X_3 are released to membrane 6.

3) MEMBRANE 6 (P SYSTEM FOR TRAINING DATA PREPARATION)

In membrane 6, the operation $X_1 \xrightarrow{R_0} X_1$ keeps the content of X_1 first. Synchronously, the operations $X_2 \xrightarrow{R_4} X_4$ and $X_3 \xrightarrow{R_4} X_5$ conduct a data augmentation approach to the basic training and validation image sets X_2 and X_3. Because deep learning methods are used in this paper and they need a lot of training data, data augmentation is applied as a data preprocessing approach to the basic data to enhance the training performance. There are many data augmentation techniques for images [79], such as image rotation, image cropping and image flipping. In this paper, based on a series of contrast tests, the rule of R_4 is finally designed with a brief 180° rotation, so the amount of the original images is doubled. Finally, membrane 6 outputs X_1, X_4, X_5 and uses them to initialize membrane 7 and 8. Till here, the work of membrane 6 is finished.

C. ENSEMBLE LEARNING

In this section, the functions and methodologies of ensemble leaning in membrane 4 are illuminated. Membrane 4 is a cell-like P system as shown in FIGURE 3, and it is used for the goal of 'feature extraction', 'feature selection' and 'ensemble learning'. This P system includes one skin membrane and 15 elementary membranes, and it is represented as Eq. (15).

$$
\begin{aligned}
\Pi_4 = (X_*, \ &\{4, 6, 7, 8, \ldots, 29\}, \ \mu_4, \ \{\omega_4 \cup \omega_6 \cup \\
&\omega_7 \cup \omega_8 \cup \ldots \cup \omega_{29}\}, \ \{R_0, \ldots, R_{22}, r_4\}), \quad (15)
\end{aligned}
$$

where its structure μ_4 is defined as Eq. (16):

$$\mu_4 = [\ [\ [\ ]_9\ [\ [\ ]_{13}\ [\ ]_{14}]_{10}]_6$$
$$[\ [\ [\ ]_{15}\ [\ ]_{16}\ [\ ]_{17}\ [\ ]_{18}\ [\ ]_{19}$$
$$[\ ]_{20}\ [\ ]_{21}\ [\ ]_{22}\ [\ ]_{23}\ [\ ]_{24}]_{11}]_7$$
$$[\ [\ [\ [\ [\ ]_{28}]_{26}\ [\ [\ ]_{29}]_{27}]_{25}]_{12}]_8]_4. \quad (16)$$

As membrane 6 is introduced in training data preparation in Sec. III-B, in this section, we focus on the contents of membrane 7 and 8. The working process of membrane 4 is shown in Algorithm 2.

1) MEMBRANE 7 (P SYSTEM FOR CLASSICAL PATTERN RECOGNITION METHODS)

Membrane 7 is introduced to select the first two optimal matching models $M_{(CPR,1)}$ and $M_{(CPR,2)}$ from multiple classical pattern recognition approaches using the rule of R_{16}, where these two models are corresponding to $Acc_{(CPR,1)}$ and $Acc_{(CPR,2)}$. In this paper, based on our prior knowledge and pre-tests [34], ten classical methods are considered and compared due to their related properties and functions, and they are introduced as follows:

(1) Membrane 15 is a P system associated with red, green, blue (RGB) color space features. x_i is a RGB image in a given image set X, where $i = 1, 2, \ldots, n$, and n is the number of images. x_i is constituted by red, green and blue color channels, namely $x_{(i,R)}$ ranging from $[0, 255]$, $x_{(i,G)}$ ranging from $[0, 255]$, and $x_{(i,B)}$ ranging from $[0, 255]$ [80]. Furthermore, the overall intensity information of x is represented by its grey-level image $x_{(i,Gr)}$. Based on the definition above, the rule of R_5 is designed with following steps: First, extract the intensity histogram of $x_{(i,R)}$, $x_{(i,G)}$, $x_{(i,B)}$, $x_{(i,Gr)}$, and each of them is represented by a 256 dimensional feature vector, $f_{(i,R)}, f_{(i,G)}, f_{(i,B)}, f_{(i,Gr)}$, respectively [78]. Finally, all the obtained feature vectors are integrated into a 1024 dimensional feature vector $f_{(i,RGB)} = [f_{(i,R)}, f_{(i,G)}, f_{(i,B)}, f_{(i,Gr)}]$. Hence, X_1 and X_5 are represented by feature matrices $F_{(S,RGB)}$ and $F_{(V,RGB)}$ using R_5, respectively, and the ith row denotes the ith feature vector in a matrix. A demonstration of R_5 is shown in FIGURE 7.

(2) Membrane 16 is a P system associated with hue, saturation, value (HSV) color space features. x_i is a HSV image in a given image set X, where $i = 1, 2, \ldots, n$, and n is the number of images. x_i is constituted by hue, saturation and blue channels, namely $x_{(i,H)}$ ranging from $[0, 360]$, $x_{(i,S)}$ ranging from $[0, 1]$ and $x_{(i,V)}$ ranging from $[0, 255]$ [81]. Based on the definition above, the rule of R_6 is designed with following steps: First, calculate the probability distribution curve of $x_{(i,H)}$, $x_{(i,S)}$, $x_{(i,V)}$, and each of them is sampled into a histogram with 100 discrete bins and represented by a 100 dimensional feature vector, $f_{(i,H)}, f_{(i,S)}, f_{(i,V)}$, respectively. Finally, all the obtained feature vectors are integrated into a 300 dimensional feature vector $f_{(i,HSV)} = [f_{(i,H)}, f_{(i,S)}, f_{(i,V)}]$. Hence, similar to membrane 15, X_1 and X_5 are represented by feature matrices $F_{(S,HSV)}$ and $F_{(V,HSV)}$ using R_6, respectively.

Algorithm 2 Workflow of Membrane 4

Input: The microscopic image set X_0.
Output: The standard image set X_1, the matching models $M_1, M_1, \ldots, M_6$.
1: Initialize membrane 4, where $S_{(4,0)} = 0$, and $G_4 = [0, 0, 0, 0]$.
2: Run membrane 6 as shown in Algorithm 1.
3: Activate membrane 4 by the output X_1, X_4, X_5 from membrane 6, and update G_4 to $[1, 0, 1, 0]$.
4: Run membrane 28 and 29, synchronously.
5: Obtain M_{DLA} and M_{DLB} from membrane 28 and 29, respectively.
6: Dissolve membrane 28 and 29 with δ and release M_{DLA} and M_{DLB} to membrane 26 and 27, respectively.
7: Run membrane 26 and 27, synchronously.
8: Obtain $(F_{(S,DLA)}, F_{(V,DLA)})$ and $(F_{(S,DLB)}, F_{(V,DLB)})$, respectively.
9: Dissolve membrane 26 and 27 with δ, and release $(F_{(S,DLA)}, F_{(V,DLA)})$ and $(F_{(S,DLB)}, F_{(V,DLB)})$ to membrane 25.
10: Run membrane 15, 16, 17, 18, 19, 20, 21, 22, 23, 24 and 25, synchronously.
11: Obtain $(F_{(S,RGB)}, F_{(V,RGB)})$, $(F_{(S,HSV)}, F_{(V,HSV)})$, $(F_{(S,HSL)}, F_{(V,HSL)})$, $(F_{(S,Lab)}, F_{(V,Lab)})$, $(F_{(S,YUV)}, F_{(V,YUV)})$, $(F_{(S,GLCM)}, F_{(V,GLCM)})$, $(F_{(S,PCA)}, F_{(V,PCA)})$, $(F_{(S,FT)}, F_{(V,FT)})$, $(F_{(S,GF)}, F_{(V,GF)})$, $(F_{(S,HOG)}, F_{(V,HOG)})$, Acc_{DLA} and Acc_{DLB}, respectively.
12: Dissolve the membranes in step 10 with δ, and release the obtained results in step 11 to membrane 11 and 12, respectively.
13: Run membrane 11 and 12, synchronously.
14: Obtain Acc_{RGB}, Acc_{HSV}, Acc_{HSL}, Acc_{Lab}, Acc_{YUV}, Acc_{GLCM}, Acc_{PCA}, Acc_{FT}, Acc_{GF}, Acc_{HOG}, and $(Acc_{(DL,1)}, M_{(DL,1)})$, synchronously.
15: Dissolve membrane 11 and 12 with δ, and release the obtained results in step 14 to membrane 7 and 8, respectively.
16: Run membrane 7 and 8, synchronously.
17: Obtain $(Acc_{(CPR,1)}, M_{(CPR,1)})$, $(Acc_{(CPR,2)}, M_{(CPR,2)})$ and $M_{DL1}, M_{DL2}, \ldots, M_{DL6}$, synchronously.
18: Dissolve membrane 7 and 8 with δ, and release $(Acc_{(CPR,1)}, M_{(CPR,1)})$, $(Acc_{(CPR,2)}, M_{(CPR,2)})$ and $M_{DL1}, M_{DL2}, \ldots, M_{DL6}$ to membrane 4, respectively.
19: **if** $Acc_{(CPR,1)}, Acc_{(CPR,2)}$ and $Acc_{(DL,1)}$ get to convergence **then** Obtain $M_1, M_2, \ldots, M_6$; otherwise, repeat step 4 to 18.
20: **end if**
21: Activate membrane 2 using $X_1, M_1, M_2, \ldots, M_6$
22: Update G_4 to $[0, 0, 0, 0]$.
23: **return** $X_1, M_1, M_2, \ldots, M_6$.

---

(3) Membrane 17 is a P system associated with hue, saturation, lightness (HSL) color space features. x_i is a HSL image in a given image set X, where $i = 1, 2, \ldots, n$, and n is the
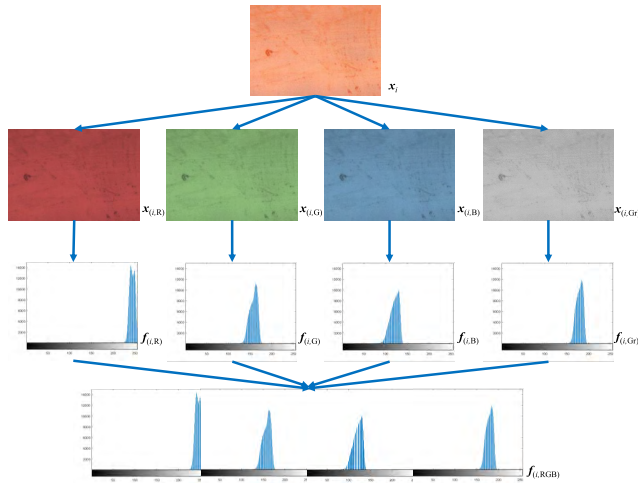
FIGURE 7. A demonstration of the proposed RGB color space features. The top row shows an original microscopic image (0 hour). The second row demonstrates the R, G, B channels and gray-level image of the original image. The third row shows the 256 bin intensity histograms of the R, G, B channels and gray-level image, respectively. The bottom row shows the integrated intensity histogram with 1024 bins.

number of images. x_i is constituted by hue, saturation and lightness channels, namely $x_{(i,H)}$ ranging from [0, 255], $x_{(i,S)}$ ranging from [0, 255] and $x_{(i,L)}$ ranging from [0, 255] [81]. Based on the definition above, the rule of R_7 is designed with following steps: First, calculate the probability distribution curve of $x_{(i,H)}$, $x_{(i,S)}$, $x_{(i,L)}$, and each of them is sampled into a histogram with 100 discrete bins and represented by a 100 dimensional feature vector, $f_{(i,H)}, f_{(i,S)}, f_{(i,L)}$, respectively. Finally, all the obtained feature vectors are integrated into a 300 dimensional feature vector $f_{(i,HSL)} = [f_{(i,H)}, f_{(i,S)}, f_{(i,L)}]$. Hence, similar to membrane 15, X_1 and X_5 are represented by feature matrices $F_{(S,HSL)}$ and $F_{(V,HSL)}$ using R_7, respectively.

(4) Membrane 18 is a P system associated with luminosity, a, b (Lab) color space features. x_i is a Lab image in a given image set X, where $i = 1, 2, \ldots, n$, and n is the number of images. x_i is constituted by L, a (green-red color components) and b (blue-yellow color components) channels, namely $x_{(i,L)}$ ranging from [0, 100], $x_{(i,a)}$ ranging from [−128, 127] and $x_{(i,b)}$ ranging from [−128, 127] [82]. Based on the definition above, the rule of R_8 is designed with following steps: First, calculate the probability distribution curve of $x_{(i,L)}$, $x_{(i,a)}$, $x_{(i,b)}$, and each of them is sampled into a histogram with 100 discrete bins and represented by a 100 dimensional feature vector, $f_{(i,L)}, f_{(i,a)}, f_{(i,b)}$, respectively. Finally, all the obtained feature vectors are integrated into a 300 dimensional feature vector $f_{(i,Lab)} = [f_{(i,L)}, f_{(i,a)}, f_{(i,b)}]$. Hence, similar to membrane 15, X_1 and X_5 are represented by feature matrices $F_{(S,Lab)}$ and $F_{(V,Lab)}$ using R_8, respectively.

(5) Membrane 19 is a P system associated with luminosity, chroma (YUV) color space features. x_i is a YUV image in a given image set X, where $i = 1, 2, \ldots, n$, and n is the number of images. x_i is constituted by Y (luma or brightness component), U and V (two chrominance or color components)

channels, namely $x_{(i,Y)}$ ranging from [0, 255], $x_{(i,U)}$ ranging from [0, 255] and $x_{(i,V)}$ ranging from [0, 255] [83]. Based on the definition above, the rule of R_9 is designed with following steps: First, calculate the probability distribution curve of $x_{(i,Y)}$, $x_{(i,U)}$, $x_{(i,V)}$, and each of them is sampled into a histogram with 100 discrete bins and represented by a 100 dimensional feature vector, $f_{(i,Y)}, f_{(i,U)}, f_{(i,V)}$, respectively. Finally, all the obtained feature vectors are integrated into a 300 dimensional feature vector $f_{(i,YUV)} = [f_{(i,Y)}, f_{(i,U)}, f_{(i,V)}]$. Hence, similar to membrane 15, X_1 and X_5 are represented by feature matrices $F_{(S,YUV)}$ and $F_{(V,YUV)}$ using R_9, respectively.

(6) Membrane 20 is a P system associated with grey-level co-occurrence matrix (GLCM) features. GLCM features consider the characteristics of the texture of an image by the statistical results of specified spatial relationship of pixel-pairs occur in an image, and it is usually used to analyze some images of materials. Hence, it is selected to extract texture features in our work. x_i is a RGB image in a given image set X, where $i = 1, 2, \ldots, n$, and n is the number of images. The rule of R_{10} is designed with following steps: First, x_i is converted into a grey-level image $x_{(i,Gr)}$. Then, with an offset of 1 in 0°, 45°, 90°, and 135° four directions, the GLCM of $x_{(i,Gr)}$ is generated [84]. Then, calculate the contrast, correlation, energy and homogeneity of these four direction, respectively. Finally, the x_i is represented by a 16 dimensional feature vector $f_{(i,GLCM)}$. Hence, similar to membrane 15, X_1 and X_5 are represented by feature matrices $F_{(S,GLCM)}$ and $F_{(V,GLCM)}$ using R_{10}, respectively.

(7) Membrane 21 is a P system associated with principle component analysis (PCA) features. In feature extraction approaches, PCA is usually used as a post-processing method for feature selection or dimensionality reduction, which can transform extracted features into new features with smaller data size but more important information. So, it is selected to analyze the principle information of images in our work. x_i is a RGB image in a given image set X, where $i = 1, 2, \ldots, n$, and n is the number of images. The rule of R_{11} is designed with following steps: First, x_i is converted into a grey-level image $x_{(i,Gr)}$. Then, the PCA approach is applied to extract a latent, which is a 256 dimensional vector containing the eigenvalues of the covariance matrix of $x_{(i,Gr)}$ [10], [85]. Thirdly, the eigenvalues in the latent are ranked in a descending order. Finally, the first 50 dimensionality of the ranked latent are selected and used as the PCA feature vector $f_{(i,PCA)}$. Hence, similar to membrane 15, X_1 and X_5 are represented by feature matrices $F_{(S,PCA)}$ and $F_{(V,PCA)}$ using R_{11}, respectively.

(8) Membrane 22 is a P system associated with Fourier transform (FT) features. FT is an effective signal processing method in pattern recognition domain, and it can represent an image by a combination of terms of lower and higher frequency, where the terms of lower frequency usually include the stronger information of the image. Hence, we choose the FT features to represent the images from the view of signal frequency analysis. x_i is a RGB image in a given image set X, where $i = 1, 2, \ldots, n$, and n is the number of images.
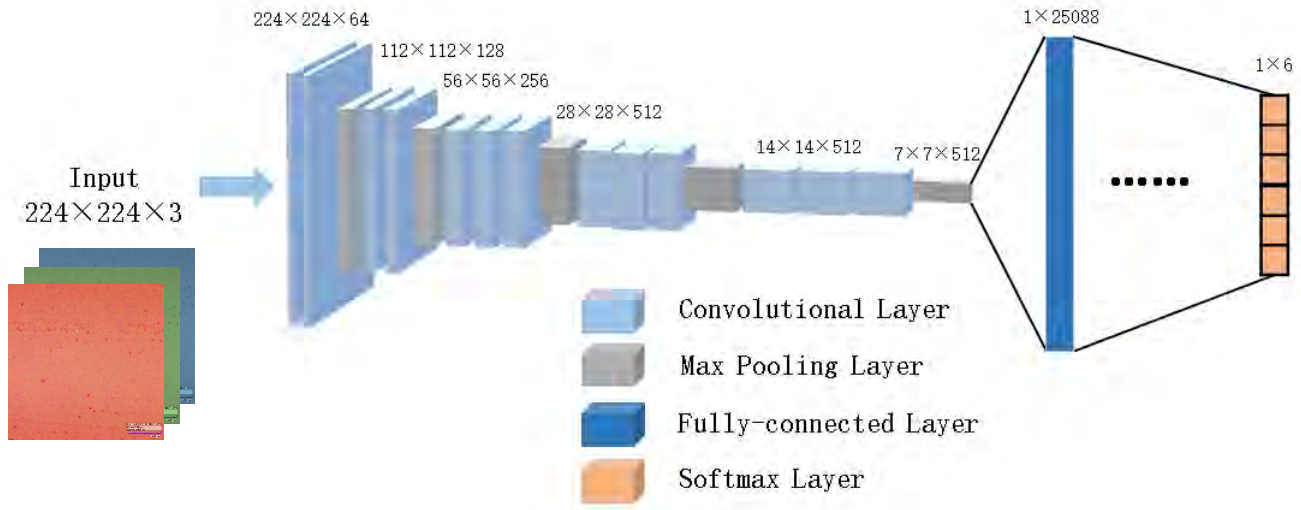
FIGURE 8. A demonstration of the selected DCNN (VGG-16 network) structure.

The rule of R_{12} is designed with following steps: First, x_i is converted into a grey-level image $x_{(i,\mathrm{Gr})}$. Then, the intensity histogram of $x_{(i,\mathrm{Gr})}$ is extracted, which is represented by a 256 dimensional vector $f_{(i,\mathrm{Gr})}$. Thirdly, discrete Fourier transform is applied to $f_{(i,\mathrm{Gr})}$ [86]. Finally, the first 50 Fourier coefficients are used as a 50 dimensional feature vector $f_{(i,\mathrm{FT})}$. Hence, similar to membrane 15, X_1 and X_5 are represented by feature matrices $F_{(\mathrm{S,FT})}$ and $F_{(\mathrm{V,FT})}$ using R_{12}, respectively.

(9) Membrane 23 is a P system associated with Gabor filter (GF) features. GFs are a series of linear filters used for texture description, which can analyze frequency and orientation information in a localized region in an image effectively. So, we choose it as a texture feature extraction approach in our work. x_i is a RGB image in a given image set X, where $i = 1, 2, \ldots, n$, and n is the number of images. The rule of R_{13} is designed with following steps: First, x_i is converted into a grey-level image $x_{(i,\mathrm{Gr})}$. Then, a set of 40 Gabor filters are designed to transform $x_{(i,\mathrm{Gr})}$ into 40 images, respectively [87]. Thirdly, for each of these 40 images, a eight bins intensity histogram is built up, so each image is represented by a eight dimensional vector $f_{(i,j)}$, where $j = 1, 2, \ldots, 40$. Finally, all 40 vectors are integrated into a 8×40 dimensional feature vector $f_{(i,\mathrm{GF})} = [f_{(i,1)}, f_{(i,2)}, \ldots, f_{(i,40)}]$. Hence, similar to membrane 15, X_1 and X_5 are represented by feature matrices $F_{(\mathrm{S,GF})}$ and $F_{(\mathrm{V,GF})}$ using R_{13}, respectively.

(10) Membrane 24 is a P system associated with histogram of orientation gradient (HOG) features. HOG is an effective local feature extraction approach, which counts occurrences of gradient orientation in local areas of an image. It can be considered as a local shape feature extraction method, as well a texture feature extraction method. Therefore, we select it to describe the characteristics of gradient changes in our work. x_i is a RGB image in a given image set X, where $i = 1, 2, \ldots, n$, and n is the number of images. The rule of

R_{14} is designed with following steps: First, x_i is converted into a grey-level image $x_{(i,\mathrm{Gr})}$. Then, a nine bins HOG of $x_{(i,\mathrm{Gr})}$ is extract [88]. Finally, x_i is represented by a nine dimensional feature vector $f_{(i,\mathrm{HOG})}$. Hence, similar to membrane 15, X_1 and X_5 are represented by feature matrices $F_{(\mathrm{S,HOG})}$ and $F_{(\mathrm{V,HOG})}$ using R_{14}, respectively.

(11) Membrane 11 is a P system associated with feature selection for classical pattern recognition methods. The rule of R_{15} is introduced to calculate the matching accuracy of each pair of standard and validation feature matrices. First, input ten pairs of feature matrices from (1) to (10) to R_{15}. Then, ten accuracies of these feature matrix pairs are obtained, namely $Acc_{\mathrm{RGB}}, Acc_{\mathrm{HSV}}, Acc_{\mathrm{HSL}}, Acc_{\mathrm{Lab}}, Acc_{\mathrm{YUV}}, Acc_{\mathrm{GLCM}}, Acc_{\mathrm{PCA}}, Acc_{\mathrm{FT}}, Acc_{\mathrm{GF}}$ and Acc_{HOG}. Finally, these obtained accuracies are released into membrane 7 for a feature selection process (Sec. IV-B).

2) MEMBRANE 8 (P SYSTEM FOR DEEP LEARNING METHODS)

Because of the effectiveness in different feature extraction tasks, a well-known DCCN structure developed by the "Visual Geometry Group (VGG)", namely VGG-16 network [89], is selected as the basic deep learning model. Furthermore, to apply VGG-16 in the degradation state matching task, a fine tuning process is handled in the fully-connected layer. The modified VGG-16 structure is shown in FIGURE 8.

(1) Membrane 28 is a P system associated with model training for deep learning method A. The rule of R_{17} is designed to directly train the parameters of a VGG-16 network using the training data set X_4 and the validation data set X_5. First, all the images in X_4 and X_5 are resized from $400 \times 300 \times 3$ to $224 \times 224 \times 3$ pixels to meet the requirement of VGG-16.

Although the resized images are 42% size of the original images, resulting in a loss of information, we still have the classical pattern recognition features from the original images to make up this loss. Hence, this image resizing operation is carried out in our work. Then, the VGG-16 structure is trained with a back propagation process [11]. Thirdly, each resized image is represented by a 25088 dimensional length feature vector in the fully-connected layer. Finally, the directly trained DCNN model M_{DLA} is obtained.

(2) Membrane 29 is a P system associated with model training for deep learning method B. The rule of R_{17} is designed to pre-train the parameters of a VGG-16 network using a transfer learning strategy. First, all the images in X_4 and X_5 are resized as that mentioned in (1). Then, the VGG-16 structure is pre-trained with a large auxiliary dataset of ImageNet [14], [15], [71]. Thirdly, a domain-specific fine-tuning process is applied to the pre-trained VGG-16 structure on the small data sets X_4 and X_5 in the fully-connected layer. Next, each resized image is represented by a 25088 dimensional length feature vector in the fully-connected layer. Finally, the indirectly trained DCNN model M_{DLB} is obtained based on the transfer learning approach.

(3) Membrane 26 is a P system associated with deep learning method A. x_i is a RGB image in a given image set X, where $i = 1, 2, \ldots, n$, and n is the number of images. The rule of R_{14} is designed with following steps: First, input x_i to the DCNN model M_{DLA}. Then, output a 25088 dimensional length feature vector f_i. Hence, similar to membrane 15, X_1 and X_5 are represented by feature matrices $F_{(S,DLA)}$ and $F_{(V,DLA)}$ using R_{18}, respectively.

(4) Membrane 27 is a P system associated with deep learning method B. x_i is a RGB image in a given image set X, where $i = 1, 2, \ldots, n$, and n is the number of images. The rule of R_{20} is designed with following steps: First, input x_i to the DCNN model M_{DLB}. Then, output a 25088 dimensional length feature vector f_i. Hence, similar to membrane 15, X_1 and X_5 are represented by feature matrices $F_{(S,DLB)}$ and $F_{(V,DLB)}$ using R_{20}, respectively.

(5) Membrane 25 is a P system associated with the first round feature selection of deep learning methods. The rule of R_{15} is applied to calculate the matching accuracy Acc_{DLA} between $F_{(S,DLA)}$ and $F_{(V,DLA)}$, and the accuracy Acc_{DLB} between $F_{(S,DLB)}$ and $F_{(V,DLB)}$, respectively. Then, these two accuracies are released into membrane 12 for a further feature selection process.

(6) Membrane 12 is a P system associated with the second round feature selection of deep learning methods. The rule of R_{16} is applied to selected the first optimal matching model $M_{(DL,1)}$ from M_{DLA} and M_{DLB}, where the selected model is corresponding to the $Acc_{(DL,1)}$. Furthermore, in membrane 8, to obtain an even robust ensemble learning performance, based on the selected DCNN model $M_{(DL,1)}$, eight hyper-parameter settings of the full-connected layer are further compared on each of the six degradation states, and the best setting for each state is selected (Sec. IV-C).

3) MEMBRANE 4 (P SYSTEM FOR ENSEMBLE LEARNING)
In membrane 4, rule $(Input_1, \ldots, Input_4) \xrightarrow{R_{22}} Output$ are specified as follows:

$Input_1$ denotes standard images X_1, $Input_2$ denotes validation images X_5, $Input_3$ denotes the set of the selected feature extraction models $\{M_{(CPR,1)}, M_{(CPR,2)}, M_{(DL,1)}\}$, $Input_4$ denotes the set of fusion weights of feature vectors $\{w_1, \ldots, w_6\}$ (Eq. (3)), and Output represents the matching models $M_{DL_1}, M_{DL_2}, \ldots, M_{DL_6}$.

In order to matching a degradation state, first, its feature vectors are extracted by the selected models $M_{(CPR,1)}$, $M_{(CPR,2)}$ and $M_{DL_1}, M_{DL_2}, \ldots, M_{DL_6}$ in Sec. III-C1 and III-C2, respectively. Hence, in each degradation state, each image becomes represented by a set Λ_i of three different features $f_{(CPR,1)}, f_{(CPR,2)}$ and $f_{DL_{i=1,2,\ldots,6}}$. Second, similarities are computed according to Eq. (5) separately for all of the feature representations in Eq. (17):

$$\Lambda_i = \begin{array}{ccc} \{f_{(CPR,1)}, & f_{(CPR,2)}, & f_{DL_i}\} \\ \downarrow & \downarrow & \downarrow \\ \psi(f_{(CPR,1)}) & \psi(f_{(CPR,2)}) & \psi(f_{DL_i}), \end{array} \quad (17)$$

where $\psi(f_{(CPR,1)})$, $\psi(f_{(CPR,2)})$ and $\psi(f_{DL_i})$ are similarities using $f_{(CPR,1)}, f_{(CPR,2)}$ and f_{DL_i}, respectively.

Furthermore, the similarities obtained above are fused by a linear combination in Eq. (18).

$$\theta(\Lambda_i) = w_{(i,1)}\psi(f_{(CPR,1)}) + w_{(i,2)}\psi(f_{(CPR,2)}) + w_{(i,3)}\psi(f_{DL_i}), \quad (18)$$

which provides an overall similarity assessment for each degradation state by Λ_i. The weight w_i indicates the usefulness of the corresponding feature vector $f_{(CPR,1)}, f_{(CPR,2)}$ and $f_{DL_{i=1,2,\ldots,6}}$ in each degradation state. If a weight is higher, then its corresponding feature is more "important".

To obtain such weights, the standard image set X_1 and validation image set X_5 are applied. Specially, a grid searching strategy is heuristically used to test possible weight combinations. First, each weight is quantized into 101 values with the step length 0.01, that is, $\{0, 0.01, 0.02, \ldots, 0.99, 1\}$. Then, in a weigh vector $w_{i=1,2,\ldots,6}$, the combination of $w_{(i,1)}, w_{(i,2)}, w_{(i,3)}$ leads to the highest matching accuracy Acc_i is selected. Finally, the selected $w_{i=1,2,\ldots,6}$ are used to implement the ensemble learning approach in membrane 4.

After all the proposed operations above, membrane 4 outputs $M_1, M_2, \ldots, M_6$ and release them to membrane 2.

D. TEST DATA PREPARATION
In this section, the usages and details of membrane 3 are introduced. Membrane 3 is a cell-like P system as shown in FIGURE 3, and it is used to prepare 'test data'. This P system includes one skin membrane and one elementary membrane, and it is represented as Eq. (19):

$$\Pi_3 = (X_*, \{3, 5\}, \mu_3, \{\omega_3 \cup \omega_5\}, \{R_4, R_{23}, r_3\}), \quad (19)$$

where its structure μ_3 is defined as Eq. (20):

$$\mu_3 = [\ [\ ]_5]_3. \quad (20)$$

Algorithm 3 Workflow of Membrane 3
___
Input: The original microscopic image set X_0.
Output: The test image set X_7.
1: Initialize membrane 3, where $S_{(6,1)} = 1$, and $G_3 = [1, 1, 0, 0]$.
2: Run membrane 5.
3: Obtain X_6 from membrane 5.
4: Dissolve membrane 5 with δ, and release X_6 to its external environment.
5: Run membrane 3.
6: Obtain X_7 from membrane 3.
7: Activate membrane 2 using X_7.
8: Update G_3 to $[0, 0, 0, 0]$.
9: **return** X_7.
___

Algorithm 4 Workflow of Membrane 2
___
Input: The microscopic image sets X_1 and X_7.
Output: The test and evaluation results $y_1, y_2, \ldots, y_6$.
1: Initialize membrane 2, where $S_{(2,1)} = 0$, and $G_2 = [0, 0, 0, 0]$.
2: Run membrane 3 and 4 as shown in Algorithm 3 and 2, synchronously.
3: Receive the released data from membrane 3 and 4, synchronously.
4: Activate membrane 2, update G_2 to $[1, 0, 0, 0]$.
5: Obtain $y_1, y_2, \ldots, y_6$ from membrane 2.
6: Dissolve membrane 2 with δ, and release $y_1, y_2, \ldots, y_6$ to its external environment.
7: Update G_2 to $= [0, 0, 0, 0]$.
8: **return** $y_1, y_2, \ldots, y_6$.
___

The working process of membrane 3 is shown in Algorithm 3.

1) MEMBRANE 5 (P SYSTEM FOR TEST DATA)

In membrane 5, the rule of $X_0 \xrightarrow{R_{23}} X_6$ works first, where except X_2 and X_3, all the remaining $(1 - p_{\text{Tr}} - p_{\text{V}})$ images in X_0 are used as test images. Then, membrane 5 is dissolved by δ, and X_6 is released to membrane 3.

2) MEMBRANE 3 (P SYSTEM FOR TEST DATA PREPARATION

In membrane 3, $X_6 \xrightarrow{R_4} X_7$ is first applied to do data augmentation on the images in X_6. Then, membrane 3 outputs X_7 and release it to membrane 2.

E. THE MATCHING MODEL

Membrane 2 is a multi-layer cell-like P system as shown in FIGURE 3, and it is used to do the final degradation state matching. This P System includes one skin membrane and 16 elementary membranes, and it is represented as Eq. (21).

$$\Pi_2 = (X_*, \{2, 3, 4, \ldots, 29\}, \mu_2, \{\omega_2 \cup \omega_3 \cup$$
$$\omega_4 \cup \ldots \cup \omega_{29}\}, \{R_0, \ldots, R_{29}, r_2\}), \quad (21)$$

where its structure μ_2 is defined as Eq. (22):

$$\mu_2 = [\ [\ [\ ]_5]_3\ [\ [\ [\ ]_9\ [\ [\ ]_{13}$$
$$[\ ]_{14}]_{10}]_6\ [\ [\ [\ ]_{15}\ [\ ]_{16}\ [\ ]_{17}$$
$$[\ ]_{18}\ [\ ]_{19}\ [\ ]_{20}\ [\ ]_{21}\ [\ ]_{22}$$
$$[\ ]_{23}\ [\ ]_{24}]_{11}]_7\ [\ [\ [\ [\ ]_{28}]_{26}$$
$$[\ [\ ]_{29}]_{27}]_{25}]_{12}]_8]_4]_2. \quad (22)$$

Because membrane 3 and 4 are well introduced in Sec. III-D and Sec. III-C, we focus on the contents of the skin membrane of this P system. The working process of membrane 2 is shown in Algorithm 4.

In membrane 2, six matching results $y_1, y_2, \ldots, y_6$ are first obtained, which are totally raw data, without any statistical significance. Then, membrane 2 outputs them to membrane 1 for further result statistics and analysis with the rules

R_{30}, R_{31} and R_{32}. In membrane 1, y_7, y_8, y_9 are the final output of the whole matching system with $i_o = 1$.

F. SUMMARY

In this section, the technical details of the proposed P system are introduced from five respects: The whole matching system in Sec. III-A, training data preparation in Sec. III-B, ensemble learning in Sec. 2, test data preparation in Sec. III-D and the matching model in Sec. III-E, referring to multiple machine vision, machine learning, pattern recognition, image processing methods.

IV. EXPERIMENTAL RESULTS AND ANALYSIS

In this section, the experimental settings (Sec. IV-A), results and analyses (Sec. IV-B, IV-C and IV-D) are introduced to show the feasibility and effectiveness of the proposed membrane computing framework. Moreover, a brief summary (Sec. IV-E) is given at the end of this section.

A. EXPERIMENTAL SETTING

1) EXPERIMENTAL DATA

In this paper, an original microscopic image data set with 1035 examples of six degradation states is used as X_0, including 150 images of 0 hour (health), 150 images of 18 hours, 195 images of 36 hours, 180 images of 54 hours, 180 images of 63 hours, and 180 images of 72 hours (failure), as the examples shown in FIGURE 1 (c) to (j). All the images are in '.png' format, with 400×300 pixel size, $3 \times 8 = 24$ bit, $3500\times$ magnification. All other image data sets are generated from X_0, and the detailed information of the experimental data is given in TABLE 3.

2) EXPERIMENTAL PROCESS

In Sec. IV-B, in order to select the feature extraction models $M_{(\text{CPR},1)}$ and $M_{(\text{CPR},2)}$, the describing abilities of ten classical pattern recognition methods mentioned in Sec. III-C1 are compared and analyzed first. Then, the effectiveness of different DCNN feature extraction approaches is

TABLE 3. The experimental data setting. The first column shows the data sets. The second column shows the total numbers of images. The third to the eighth columns represent the degradation states. The last two columns show the corresponding P system rules and describitions.

Image set	Total	0 h	18 h	36 h	54 h	63 h	72 h	Rule	Description
Original images: X_0	1035	150	150	195	180	180	180	–	An original microscopic image data set.
Standard images: X_1	6	1	1	1	1	1	1	$R_1, \kappa_s = 50$	An example is shown in FIGURE 6.
Training images: X_2	207	30	30	39	36	36	36	$R_2, p_{\text{Tr}} = 20\%$	Training data.
Validation images: X_3	517	75	75	97	90	90	90	$R_3, p_{\text{V}} = 50\%$	Validation data.
Training images: X_4	414	60	60	78	72	72	72	$R_4, 180°$ rotation	Data augmentation.
Validation images: X_5	1035	150	150	195	180	180	180	$R_4, 180°$ rotation	Data augmentation.
Test images: X_6	311	45	45	59	54	54	54	$R_{23}, 1 - p_{\text{Tr}} - p_{\text{V}} = 30\%$	Test data.
Test images: X_7	622	90	90	118	108	108	108	$R_4, 180°$ rotation	Data augmentation.

evaluated in Sec. IV-C to select a better performance on $M_{(\text{DL},1)}$ mentioned in Sec. III-C2. Furthermore, the models $M_{\text{DL}_1}, M_{\text{DL}_2}, \ldots, M_{\text{DL}_6}$ are selected for each degradation state. Lastly, the final obtained matching models using ensemble learning, $M_1, M_2, \ldots, M_6$, are tested to demonstrate the usefulness of the proposed membrane computing framework in this paper.

B. EVALUATION OF CLASSICAL PATTERN RECOGNITION METHODS

In this section, the functions of classical pattern recognition methods in membrane 7 (Sec. III-C1) are proved using X_1 and X_5.

(1) In order to select the first two optimal feature extraction models $M_{(\text{CPR},1)}$ and $M_{(\text{CPR},2)}$ from ten methods mentioned in Sec. III-C1, the matching accuracies are compared in FIGURE 9.
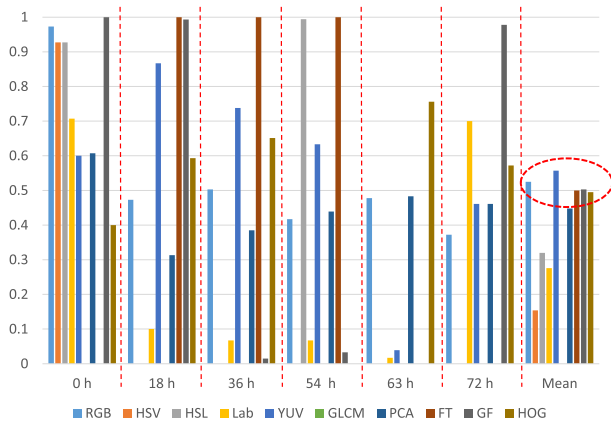

FIGURE 9. A comparison of the matching accuracies using ten classical pattern recognition feature extraction approaches on the validation data set. The horizontal axis shows different feature extraction approaches (RGB, HSV, HSL, Lab, YUV, GLCM, PCA, FT, GF and HOG) at different degradation states and their overall performance (mean accuracies). The vertical axis denotes the matching accuracies of different approaches. In the red dotted circle, five feature extraction methods obtained close accuracies around 50%.

As shown in FIGURE 9, the analysis of different feature extraction methods is discussed below:

1) The RGB feature has a high matching accuracy of 97.3% at 0 hour, and medium results at other states. Finally, the RGB feature shows an available and stable

performance in the state matching task. Similar to the RGB feature, the YUV, HOG and PCA feature have higher mean accuracies and stable matching abilities. The YUV feature even obtains the highest mean accuracy of 55.6% among all ten compared methods.

2) For FT and GF features, both of them have higher mean matching accuracies around 50%, but their matching performance in different states are quite different, showing their lower working stabilities. Hence, the usages of these two approaches are limited in practice.

3) The HSV, HSL and Lab features only have good performance in certain states, like 0, 54 and 72 hours, but loose efficacy in other states. Due to their lower mean accuracies and stabilities, they are not suitable for this matching task.

4) For the GLCM feature, due to the standard images have a contrast near to 0, which totally destroys the describing ability of the feature, resulting in a failed result. However, this poor performance of the GLCM feature is not caused by the feature extraction method itself, but shows that the usage of the GLCM is not suitable for this matching task.

(2) As shown in FIGURE 9, because five feature extraction methods, RGB, YUV, FT, GF and HOG, obtain high and close accuracies around 50%, the operation of 'practical case' in the rule R_{16} is applied. Hence, the variances of these five methods are further compared in FIGURE 10.

From FIGURE 10, the most stable two feature extraction methods, the RGB and HOG features, are selected. Based on the rule of R_{16}, because RGB and HOG features have the first and second lowest variances, the feature extraction models $M_{(\text{CPR},1)}$ and $M_{(\text{CPR},2)}$ are referring to them, respectively. In FIGURE 11 and 12, the details of the matching result using the $M_{(\text{CPR},1)}$ model (the RGB feature) and $M_{(\text{CPR},2)}$ model (the HOG feature) are shown in two confusion matrices, respectively.

From FIGURE 11 and 12, a distinct complementarity between the $M_{(\text{CPR},1)}$ (RGB) and $M_{(\text{CPR},2)}$ (HOG) is shown. For example, the $M_{(\text{CPR},1)}$ obtains a matching accuracy of 97.3% at the 0 hour, and the $M_{(\text{CPR},2)}$ only has a accuracy of 40%. In contrast, at 72 hours, the $M_{(\text{CPR},1)}$ only obtains 41.7% accuracy, but the $M_{(\text{CPR},2)}$ is 20% higher. Hence, this complementarity provides a higher possibility for a further ensemble learning.
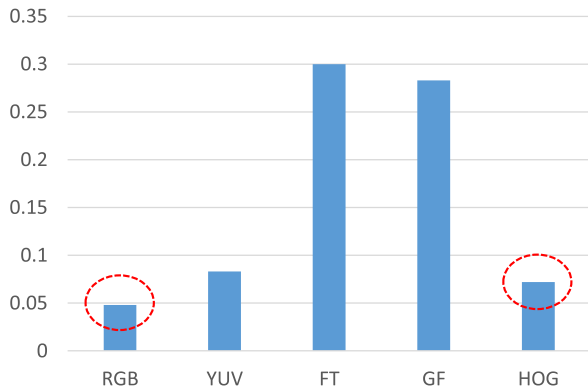
FIGURE 10. A comparison of the variances of matching accuracies using five classical pattern recognition feature extraction approaches on the validation data set. The horizontal axis shows different approaches (RGB, YUV, FT, GF and HOG). The vertical axis denotes the variances of matching accuracies of different approaches. In the red dotted circles, the most stable two feature extraction methods are found by the lowest two variances.

Actual Degradation State

	0 h	18 h	36 h	54 h	63 h	72 h	Sum	Acc (%)
0 h	146	0	0	2	2	0	150	97.3
18 h	3	71	27	2	35	12	150	47.3
36 h	8	17	98	35	19	18	195	50.3
54 h	1	7	34	75	45	18	180	41.7
63 h	0	4	13	37	86	40	180	47.8
72 h	0	1	21	33	58	67	180	37.2

Matched Degradation State

FIGURE 11. The confusion matrix of the state matching result by the $M_{(CPR,1)}$ model (the RGB feature) on the validation data set. The mean accuracy is 52.5% and variance is 4.8%.

Actual Degradation State

	0 h	18 h	36 h	54 h	63 h	72 h	Sum	Acc (%)
0 h	60	1	39	19	31	0	150	40
18 h	25	89	6	28	2	0	150	59.3
36 h	34	8	127	18	0	8	195	65.1
54 h	62	5	0	0	88	25	180	0
63 h	0	3	32	7	136	2	180	75.6
72 h	0	4	48	3	22	103	180	57.2

Matched Degradation State

FIGURE 12. The confusion matrix of the state matching result by the $M_{(CPR,2)}$ model (the HOG feature) on the validation data set. The mean accuracy is 49.5% and the variance is 7.2%.

FIGURE 13. A comparison of the matching accuracies using two deep learning feature extraction approaches on the validation data set. The horizontal axis shows different approaches (directly trained VGG-16 and pre-trained VGG-16 using transfer learning) at different degradation states and their overall performance (mean accuracies). The vertical axis denotes the matching accuracies of different approaches. The red dotted circle, marks the method with the highest accuracy.

C. EVALUATION OF DEEP LEARNING METHODS

In this part, the usefulness of the deep learning methods in membrane 8 (Sec. III-C2) is tested using X_1 and X_5.

(1) In order to select the first optimal deep learning feature extraction model $M_{(DL,1)}$ from two DCNN structures mentioned in Sec. III-C2, the matching accuracies are compared in FIGURE 13.

As shown in FIGURE 13, the analysis of two feature extraction methods is discussed below:

1) Due to the small data set problem, it is very difficult to train an effective deep learning (VGG-16) structure directly, resulting in a poor state matching accuracy of 15.3%.

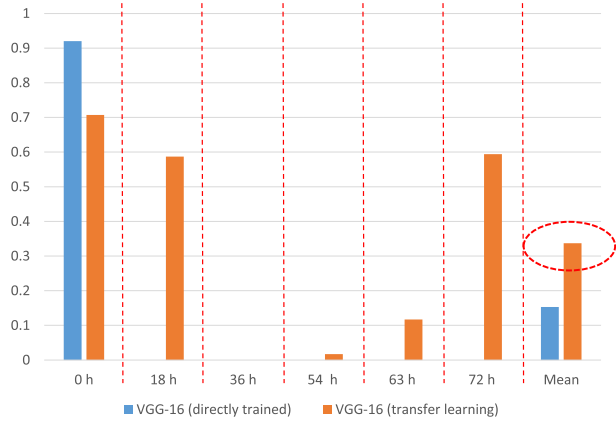2) In contrast to the directly trained deep learning (VGG-16) structure, the transfer learning strategy enhances the deep learning (VGG-16) method with a doubled accuracy of 33.7%, showing a great improvement.

(2) As shown in FIGURE 13, because the pre-trained deep learning (VGG-16) using transfer learning obtains a much higher matching accuracy than the directly trained one, the operation of 'ideal case' in the rule R_{16} is applied. Hence, the method of deep learning (VGG-16) using transfer learning is selected as the deep learning feature extraction model $M_{(DL,1)}$. In addition, the details of the matching result using the $M_{(DL,1)}$ is shown in FIGURE 14.

Furthermore, based on the selected deep learning model $M_{(DL,1)}$ and the rule of R_{21}, eight hyper-parameter settings are tested in the softmax layer in FIGURE 8 for a fine tune, including 6, 16, 64, 256, 1024 and 2048 dimensional length

Actual Degradation State

	0 h	18 h	36 h	54 h	63 h	72 h	Sum	Acc (%)
0 h	**106**	44	0	0	0	0	150	70.7
18 h	19	**88**	0	0	8	35	150	58.7
36 h	28	84	**0**	0	4	79	195	0
54 h	20	20	3	**3**	4	130	180	1.7
63 h	10	46	0	0	**21**	103	180	11.7
72 h	10	55	0	3	5	**107**	180	59.4

(Matched Degradation State)

FIGURE 14. The confusion matrix of the state matching result by the $M_{(DL,1)}$ model (VGG-16 using transfer learning) on the validation data set. The mean accuracy is 33.7% and variance is 10.6%.

TABLE 4. The selected optimal hyper-parameters used in the $M_{(DL,1)}$ for different matching states. The first row shows the degradation states. The second row shows the hyper-parameters.

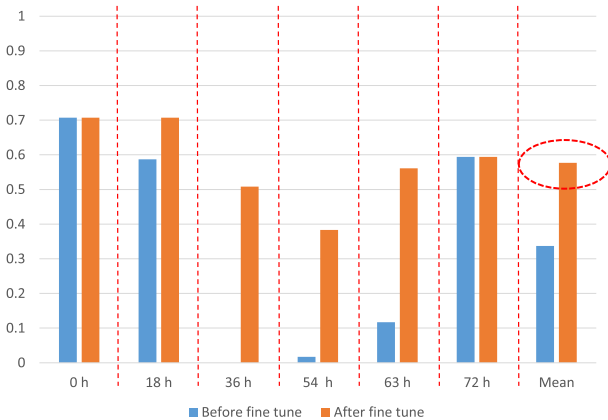| State	0 h	18 h	36 h	54 h	63 h	72 h
Hyper-parameter	6	16	512	2048	2048	6

FIGURE 15. A comparison of the matching accuracies using $M_{(DL,1)}$ before and after the fine tune on the validation data set. The horizontal axis shows different approaches ($M_{(DL,1)}$ before and after fine tune) at different degradation states and their overall performance (mean accuracies). The vertical axis denotes the matching accuracies of different approaches. In the red dotted circle, the method obtains a higher accuracy is marked.

feature vectors. In TABLE 4, the selected optimal hyper-parameters for different degradation states are given.

To evaluate the effectiveness of the fine tune work above, a comparison of the matching accuracies is shown in FIGURE 15, where after fine tuning the models ($M_{DL_1}, M_{DL_2}, \ldots, M_{DL_6}$) are obtained. Using the fine tuned models, a mean accuracy which is 24% higher than that before fine tuning. In addition, the details of the matching result is shown in FIGURE 16.

Actual Degradation State

	0 h	18 h	36 h	54 h	63 h	72 h	Sum	Acc (%)
0 h	**106**	44	0	0	0	0	150	70.7
18 h	4	**106**	6	10	11	13	150	70.7
36 h	14	38	**99**	6	13	25	195	50.8
54 h	14	3	24	**69**	62	8	180	38.3
63 h	5	28	14	14	**101**	18	180	56.1
72 h	11	54	0	3	5	**107**	180	59.4

(Matched Degradation State)

FIGURE 16. The confusion matrix of the state matching result by the $M_{(DL,1)}$ model after fine tune on the validation data set. The mean accuracy is 57.7% and variance is 4.3%.

D. EVALUATION OF THE ENSEMBLE LEARNING APPROACH

In this section, the proposed ensemble learning using a membrane computing framework in membrane 4 (Sec. III-C3) is tested using X_1 and X_5.

(1) To obtain matching models $M_1, M_2, \ldots, M_6$, the selected feature extraction models $M_{(CPR,1)}$, $M_{(CPR,2)}$, $M_{DL_1}, M_{DL_2}, \ldots, M_{DL_6}$, are fused together with the weights $w_1, w_1, \ldots, w_6$ using the rule of R_{22}. These weights are shown in TABLE 5.

TABLE 5. Fusion weights used in the ensemble learning process. The first column shows different matching models. The first row denotes the fusion weights.

	w_1	w_2	w_3	w_4	w_5	w_6
$M_{(CPR,1)}$	**0.525**	**0.525**	0.000	0.113	0.010	0.000
$M_{(CPR,2)}$	0.300	0.300	**1.000**	0.100	**0.900**	0.000
M_{DL_1}	0.175	–	–	–	–	–
M_{DL_2}	–	0.175	–	–	–	–
M_{DL_3}	–	–	0.000	–	–	–
M_{DL_4}	–	–	–	0.787	–	–
M_{DL_5}	–	–	–	–	0.090	–
M_{DL_6}	–	–	–	–	–	**1.000**
Sum	1.000	1.000	1.000	1.000	1.000	1.000

(2) Using the obtained fusion weights $w_1, w_1, \ldots, w_6$ above, the matching accuracies of the ensemble learning approach is compared to the single models $M_{(CPR,1)}$ (RGB), $M_{(CPR,2)}$ (HOG) and $M_{DL_1}, M_{DL_2}, \ldots, M_{DL_6}$ (VGG-16 using transfer learning and fine tune) in FIGURE 17.

As shown in FIGURE 17, the matching result using the ensemble learning strategy exceeds the results using all the single models ($M_{(CPR,1)}$, $M_{(CPR,2)}$ and $M_{DL_1}, M_{DL_2}, \ldots, M_{DL_6}$). In addition, the details of the matching result is shown in FIGURE 18.

(3) Finally, the whole P system (membrane 1) is tested using X_7 and the rule of R_{30} to R_{32}, and the details of the matching result is shown in FIGURE 19.
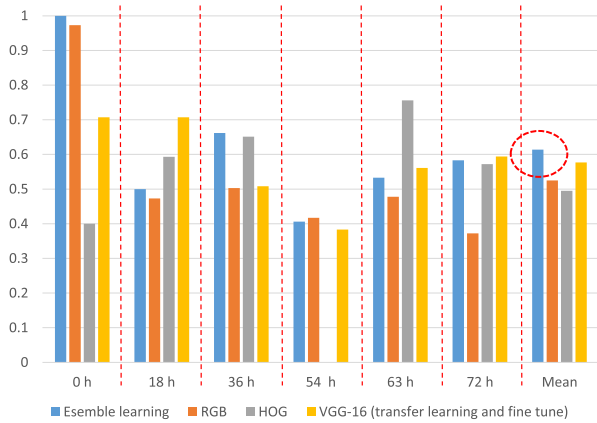
FIGURE 17. A comparison of the matching accuracies using ensemble learning and single models. The horizontal axis shows different approaches ($M_{(CPR,1)}$ (RGB), $M_{(CPR,2)}$ (HOG) and M_{DL_1}, M_{DL_2}, ..., M_{DL_6} (VGG-16 using transfer learning and fine tune) at different degradation states and their overall performance (mean accuracies) on the validation data set. The vertical axis denotes the matching accuracies of different approaches. The red dotted circle shows the method with the highest accuracy.

Actual Degradation State

	0 h	18 h	36 h	54 h	63 h	72 h	Sum	Acc (%)
0 h	150	0	0	0	0	0	150	100
18 h	9	75	21	16	23	6	150	50
36 h	0	11	129	33	14	8	195	66.2
54 h	0	6	44	73	38	19	180	40.6
63 h	0	17	51	2	96	14	180	53.3
72 h	9	58	0	3	5	105	180	58.3

(Matched Degradation State)

FIGURE 18. The confusion matrix of the state matching result by the ensemble learning strategy on the validation data set. The mean accuracy is 61.4% and variance is 4.3%.

Actual Degradation State

	0 h	18 h	36 h	54 h	63 h	72 h	Sum	Acc (%)
0 h	90	0	0	0	0	0	90	100
18 h	5	44	13	10	14	4	90	48.9
36 h	0	7	77	21	8	5	118	65.3
54 h	0	5	25	44	23	11	108	40.7
63 h	0	10	31	1	58	8	108	53.7
72 h	5	35	0	3	3	62	108	57.4

(Matched Degradation State)

FIGURE 19. The confusion matrix of the state matching result in the final test for membrane 1 on the test data set. The mean accuracy is 61.0% and variance is 4.3%.

(a) 0 hour (healthy)

(b) 18 hours

(c) 36 hours

(d) 54 hours

(e) 63 hours

(f) 72 hours (failure)

FIGURE 20. A demonstration of the Gaussian distribution in membrane 1 on the test data set. (a) to (f) show the actual degradation states, respectively. The horizontal axis in each sub-figure shows the matched degradation states. The vertical axis in each sub-figure denotes the matching results. The red curves are the fitting results in a Gaussian distribution.

As shown in FIGURE 19, the proposed method achieves a higher accuracy of 61.0% than that using all the single approaches on the test data set with the single state matching case, showing the effectiveness of our method. Furthermore, membrane 1 shows a distinct trend of Gaussian distribution. Hence, in a practical work, membrane 1 is not only useful to match a new microscopic image to a certain single degradation state, but also useful to match the new image to a range of nearby degradation states. A demonstration of the Gaussian distribution trend is shown in FIGURE 20.

From FIGURE 20, we can find that, if we consider each three neighboring states as a state range, and define the state of the middle one as the state of this range, then we can achieve the accuracy of state range matching as shown in FIGURE 21.
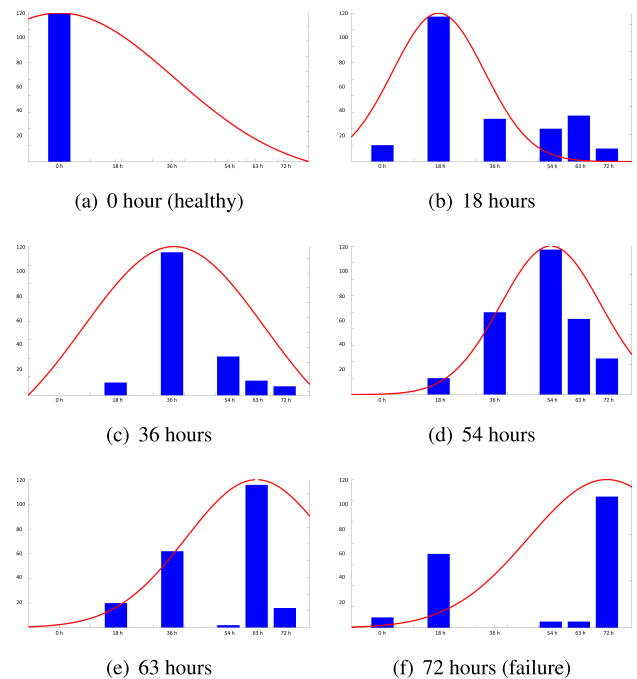
From FIGURE 21, we can find that, the state matching result achieves an accuracy of 77.4% and a variance of 2.6%, showing a good matching performance and a high stability. Furthermore, we compare the matching results between our proposed method and human visual analysis of the images. Especially, three human matching results are obtained, and their average can be used as a benchmark of performance for the automated system. The comparison is shown in FIGURE 22.
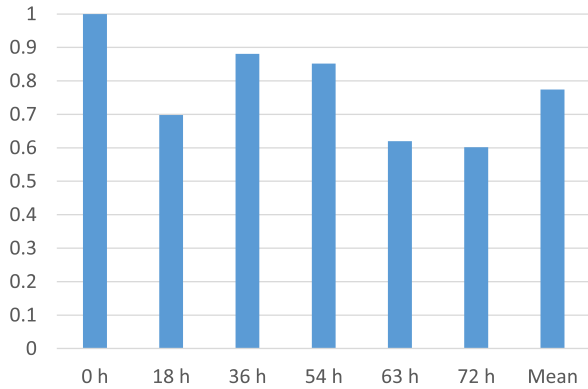
FIGURE 21. The state range matching result (accuracy) on the test data set. The horizontal axis shows six degradation states and mean result. The vertical axis shows the matching results. The mean accuracy is 77.4% and variance is 2.6%.
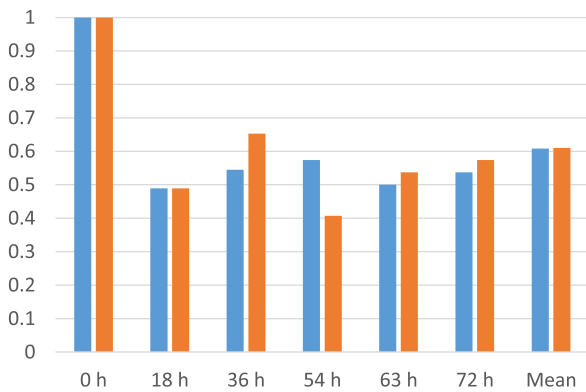

FIGURE 22. A comparison of matching results (accuracy) between human average and our proposed method on the test data set. The horizontal axis shows six degradation states and mean result of human and our method, where the blue bins on the left side denote the human average, and the original bins on the right side represent our method. The vertical axis shows the matching results. The mean accuracy of human average is 60.8% and variance is 3.2%. The mean accuracy of our method is 61.0% and variance is 4.3%.

From FIGURE 22, we can find that the matching performance of our proposed method (61.0% accuracy) is very close to the human matching result (60.8% accuracy), proving the effectiveness of our method. However, the variance of our method is 1.1% higher than the human average, showing the stability of our method is lower than the human work.

Finally, when we apply the proposed system in a real-world environment: First, the similarity between a new test image and each of the six standard images is automatically calculated using the matching models of $M_1, M_2, \ldots, M_6$, respectively. Then, the test image is matched to the state with the highest similarity. Hence, the users only need to give one test image to the system, but do not need to choose any models or weights manually.

E. SUMMARY

In this section, the proposed ensemble learning system using a membrane computing framework is tested to prove the

usefulness and effectiveness. First, the experimental setting is introduced in Sec. IV-A. Then, two feature extraction approaches using RGB and HOG methods are selected in Sec. IV-B. Thirdly, a transfer learning based VGG-16 network is selected in Sec. IV-C. Finally, the ensemble learning approach is tested in Sec. IV-D, and achieves 61.0% and 77.4% accuracies on the test data set with single state matching and state range matching, respectively.

V. HARDWARE DESIGN

In order to apply the proposed microscopic machine vision system in practical industrial fields, a corresponding hardware is designed.

A. ADDRESSED PROBLEMS

Low-voltage electromagnetic coil is a device that uses the principle of electromagnetic induction to work. There are many factors affecting the working performance of the coil, including the coil material (e.g., copper and aluminum), the number of winding turns, and the working environmental conditions (e.g., temperature, humidity and dust). To avoid the influence from the working environments, the coils are usually protected by some insulated rubber tapes, as shown in FIGURE 23.
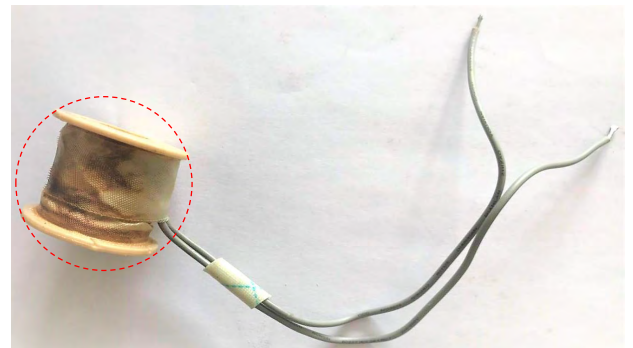

FIGURE 23. An example of the a coil that is protected by some insulated rubber tapes (the part in the red dotted circle).

Because the insulated rubber tapes are always thick, solid and non-transparent, it is not possible to apply the proposed microscopic machine vision system to monitor the degradation states during the use of the coil in practical work. Hence, a novel mechanical device is designed, considering the external protection and visible monitoring problems from the following respects jointly:

(1) The materials of the mechanical device itself is insulated.
(2) The mechanical device can isolate the influence of the working environment.
(3) The mechanical device is able to rotate to observe the 360° changes of the wire throughout the coil.
(4) An observing port is designed to connect with the observation lens from a microscopy.

B. DESIGNING

1) MATERIALS OF THE MECHANICAL DEVICE

Because the working environment as of the coils are usually with high temperature, high humidity and dusty conditions, some widely used engineering materials, like 'polyamide' (PA) [90], are considered. Hence, based on the prior knowledge and experiences, the following materials are selected as follows: The main shaft of the coil uses 'poly tetra fluoroethylene' (PTFE); the bearings, nut, and sleeves use PA; the upper lids, lower lids, and the end caps use 'acrylonitrile butadiene styrene' (ABS); the observation window uses 'polyvinyl chloride' (PVC); the gaskets and seals use 'fluorelastomer'. These selected materials have some common properties in practical work, including lightness, waterproof, heat resistant, insulated, strong, wear resistant, good plasticity and anti-magnetic electricity.
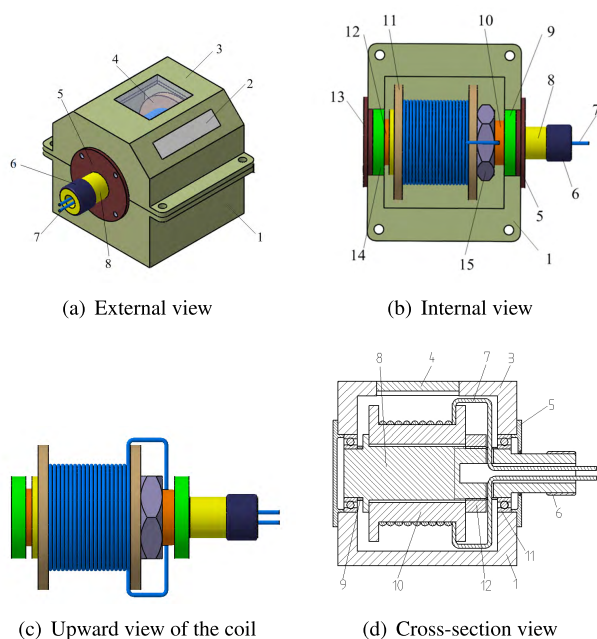

FIGURE 24. A demonstration of the designed structure for the mechanical device to protect and monitor a coil. (a) is the external view, (b) is the internal view, (c) is the upward view of the coil, and (d) is the cross-section view. Component No.: 1. lower cover, 2. optical screen, 3. upper cover, 4. observation window, 5. front cover, 6. handle, 7. wire, 8. spindle, 9. front bearing, 10. front axle sleeve, 11. spool, 12. rear axle sleeve, 13. rear end cap, 14. rear bearing, 15. nut.

2) STRUCTURE OF THE MECHANICAL DEVICE

Considering all the needed functions, the mechanical device is designed as shown in FIGURE 24.

In FIGURE 24, the upper cover No. 3 and the lower cover No. 1 in the system are connected by four bolts, and a rubber gasket is interposed in the middle. The front and rear end covers No. 5 and No. 13 are also connected to the upper and lower covers by bolts, and the end cover and the shaft contact with seal grooves which is used to install seals to ensure that the system is isolated from the external environment. The bobbin No. 11 of the coil is sleeved on the main shaft No. 8,

and the entire coil is fixed on the shaft by the nut No. 15. The main shaft No. 8 is hollow, and the electric wire passes through the front shaft sleeve No. 10 and the through hole on the main shaft No. 8 to connect the external power supply. The main shaft is matched with the upper and lower covers No. 3 and No. 1 through the front and rear bearings No. 9 and No. 14 to achieve the purpose of driving the coil to rotate. The observation window No. 4 and the screen No. 2 are designed on the upper cover No. 3 to achieve the purpose of observation using an outer lens of a microscopy.

C. SUMMARY

In order to monitor the degradation states of the low-voltage electromagnetic coil insulation using the proposed microscopic machine vision system in this paper, a mechanical device is designed. First, the materials of this mechanical system are selected referring to the properties of insulated, anti-electromagnetic, high temperature (Sec. V-B1). Then, this mechanical device not only plays a protective role against heating, water and dust, but also realizes the purpose of 360° rotating the coil for an overall observing (Sec. V-B).

VI. CONCLUSION AND FUTURE WORK

This work is an interdisciplinary research, referring to computer science (machine vision, machine learning and membrane computing), reliability engineering (degradation monitoring) and industrial design (mechanical system design), which provides a novel, interesting and potential topic for both scientific and industrial fields.

A. CONCLUSION

In this paper, a novel microscopic machine vision system is proposed to solve a degradation monitoring problem of low-voltage electromagnetic coil insulation, where an ensemble learning approach using a membrane computing framework is creatively introduced. In Sec. I, the whole system is introduced first. Then, related works of degradation monitoring, microscopic machine, ensemble learning, membrane computing, classical pattern recognition methods, and deep learning methods are briefly reviewed in Sec. II. Thirdly, the details of the proposed algorithms are introduced in Sec. III, including the definition of the whole membrane system and the usages of it for the ensemble learning. In Sec. IV, experiments are used to evaluate and attest the usefulness and potential of the proposed system, where a mean accuracy of $61, 4\%$ is achieved on the validation data set of six degradation states with single state matching. Furthermore, 61.0% and 77.4% accuracies are achieved on the test data set with state range matching. Finally, in order to apply the proposed microscopic machine vision system in a practical work in Sec. V, a hardware (a mechanical device) is designed to replace the current used insulated rubber tapes from the coils.

B. FUTURE WORK

Because this work is the first one to use machine vision, ensemble learning and membrane computing approaches in

a degradation monitoring task, it provides a very huge potential for the future research. Besides the degradation monitoring for the low-voltage electromagnetic coil insulation, some other related cases, such as metal fatigue [91] and concrete aging [92], can be also monitored by similar methods. As well, more advanced machine learning methods, such as the 'generative adversarial networks' (GAN) [93] and graph theory based methods [94], can be included in the membrane computing framework for a more accurate matching result. In addition, more self-adaptive functions, like the nove global numerical optimization [95] and the adaptive regularization method [96], can be inserted into the membrane computing systems for a more rapid and robust matching result. Furthermore, more exquisite designs, as the electronic cluster eyes [97] and wireless sensors [98], are possible to make the system as a part of the internet of things. In addition, we only apply the most basic similarity matching strategy in this paper, without any machine learning algorithms, so we consider to introduce some advantaged machine learning approaches to improve the matching performance, like artificial neural network [11], random forests [99] and conditional random fields [63].

REFERENCES

[1] N. J. Jameson, M. H. Azarian, and M. Pecht, "Impedance-based condition monitoring for insulation systems used in low-voltage electromagnetic coils," *IEEE Trans. Ind. Electron.*, vol. 64, no. 5, pp. 3748–3757, May 2017.

[2] Motor Reliability Working Group, "Report of large motor reliability survey of industrial and commercial installations, Part I," *IEEE Trans. Ind. Appl.*, vol. IA-21, no. 4, pp. 853–864, Jul. 1985.

[3] Motor Reliability Working Group, "Report of large motor reliability survey of industrial and commercial installations, Part II," *IEEE Trans. Ind. Appl.*, vol. IA-21, no. 4, pp. 865–872, Jul. 1985.

[4] O. V. Thorsen and M. Dalva, "A survey of faults on induction motors in offshore oil industry, petrochemical industry, gas terminals, and oil refineries," *IEEE Trans. Ind. Appl.*, vol. 31, no. 5, pp. 1186–1196, Sep. 1995.

[5] P. J. Tavner, "Review of condition monitoring of rotating electrical machines," *IET Electr. Power Appl.*, vol. 2, no. 4, pp. 215–247, Jul. 2008.

[6] V. P. Bacanskas, G. C. Roberts, and G. J. Toman, "Aging and service wear of solenoid-operated valves used in safety systems of nuclear power plants: Operating experience and failure identification," Franklin Res. Center, Oak Ridge Nat. Lab., Nucl. Regulatory Commission, Philadelphia, PA, USA, Tech. Rep. NUREG/CR–4819, 1987, vol. 1.

[7] *Hydrogenerator Failures-Results of the Survey*, document GIGRE Study Committee SC11, EG11.02, 2002.

[8] W. C. Sant'Ana, C. P. Salomon, G. Lambert-Torres, L. E. B. da Silva, E. L. Bonaldi, L. E. de Lacerda de Oliveira, and J. G. B. da Silva, "Early detection of insulation failures on electric generators through online frequency response analysis," *Electr. Power Syst. Res.*, vol. 140, pp. 337–343, Nov. 2016.

[9] C. M. Bishop, *Pattern Recognition and Machine Learning*. New York, NY, USA: Springer, 2006.

[10] S. Theodoridis and K. Koutroumbas, *Pattern Recognition*, 4th ed. Amsterdam, The Netherlands: Elsevier, 2009.

[11] M. Nielsen, *Neural Networks and Deep Learning*. Determination Press, 2015. [Online]. Available: http://neuralnetworksanddeeplearning.com/

[12] J. Gu, Z. Wang, J. Kuen, L. Ma, A. Shahroudy, B. Shuai, T. Liu, X. Wang, G. Wang, J. Cai, and T. Chen, "Recent advances in convolutional neural networks," *Pattern Recognit.*, vol. 77, pp. 354–377, May 2018.

[13] K. Shirahama, Y. Matsuoka, and K. Uehara, "Event retrieval in video archives using rough set theory and partially supervised learning," *Multimedia Tools Appl.*, vol. 57, no. 1, pp. 145–173, 2012.

[14] K. Chatfield, K. Simonyan, A. Vedaldi, and A. Zisserman, "Return of the devil in the details: Delving deep into convolutional nets," 2014, *arXiv:1405.3531*. [Online]. Available: https://arxiv.org/abs/1405.3531

[15] R. Girshick, J. Donahue, T. Darrell, and J. Malik, "Rich feature hierarchies for accurate object detection and semantic segmentation," in *Proc. CVPR*, Jun. 2014, pp. 580–587.

[16] D. Opitz and R. Maclin, "Popular ensemble methods: An empirical study," *J. Artif. Intell. Res.*, vol. 11, pp. 169–198, Aug. 1999.

[17] R. Polikar, "Ensemble based systems in decision making," *IEEE Circuits Syst. Mag.*, vol. 6, no. 3, pp. 21–45, Sep. 2006.

[18] L. Rokach, "Ensemble-based classifiers," *Artif. Intell. Rev.*, vol. 33, nos. 1–2, pp. 1–39, 2010.

[19] L. Breiman, "Bias, variance, and arcing classifiers," Univ. California, Berkeley, CA, USA, Tech. Rep. 460, 1996.

[20] Z.-H. Zhou, *Ensemble Methods: Foundations and Algorithms*. London, U.K.: Chapman & Hall, 2012.

[21] G. Ciobanu, M. Pérez-Jiménez, and G. Păun, *Applications of Membrane Computing*. Berlin, Germany: Springer, 2006.

[22] P. Frisco, M. Gheorghe, and M. Pérez-Jiménez, *Applications of Membrane Computing in Systems and Synthetic Biology*. Cham, Switzerland: Springer, 2014.

[23] J. Dassow and G. Păun, "On the power of membrane computing," *J. Universal Comput. Sci.*, vol. 5, no. 2, pp. 33–49, 1999.

[24] P. Werynski, D. Roger, R. Corton, and J. F. Brudny, "Proposition of a new method for in-service monitoring of the aging of stator winding insulation in AC motors," *IEEE Trans. Energy Convers.*, vol. 21, no. 3, pp. 673–681, Sep. 2006.

[25] F. Perisse, P. Werynski, and D. Roger, "A new method for AC machine turn insulation diagnostic based on high frequency resonances," *IEEE Trans. Dielectr. Electr. Insul.*, vol. 14, no. 5, pp. 1308–1315, Oct. 2007.

[26] F. Perisse, D. Mercier, E. Lefevre, and D. Roger, "Robust diagnostics of stator insulation based on high frequency resonances measurements," *IEEE Trans. Dielectr. Electr. Insul.*, vol. 16, no. 5, pp. 1496–1502, Oct. 2009.

[27] S. Savin, S. Ait-Amar, D. Roger, and G. Vélu, "Aging effects on the AC motor windings: A correlation between the variation of turn-to-turn capacitance and the PDIV," in *Proc. CEIDP*, Oct. 2011, pp. 64–67.

[28] S. Savin, S. Ait-Amar, and D. Roger, "Turn-to-turn capacitance variations correlated to PDIV for AC motors monitoring," *IEEE Trans. Dielectr. Electr. Insul.*, vol. 20, no. 1, pp. 34–41, Feb. 2013.

[29] C. Zoeller, T. Winter, T. M. Wolbank, and M. A. Vogelsberger, "Detection of AC machines insulation health state based on evaluation of switching transients using two current sensors and eigenanalysis-based parameter estimation," in *Proc. ECCE*, Sep. 2014, pp. 3111–3118.

[30] C. Zoeller, T. M. Wolbank, and M. A. Vogelsberger, "Online insulation condition monitoring of traction machines using inverter induced voltage injection," in *Proc. IECON*, Nov. 2015, pp. 2456–2462.

[31] C. Zoeller, T. M. Wolbank, and M. A. Vogelsberger, "Influence of voltage excitation and current sensors on monitoring of stator winding insulation based on transient current step response," in *Proc. ECCE*, Sep. 2015, pp. 2854–2861.

[32] P. Nussbaumer, M. A. Vogelsberger, and T. M. Wolbank, "Induction machine insulation health state monitoring based on online switching transient exploitation," *IEEE Trans. Ind. Electron.*, vol. 62, no. 3, pp. 1835–1845, Mar. 2015.

[33] N. J. Jameson, K. Wang, C. Morillo, M. H. Azarian, and M. Pecht, "Health monitoring of solenoid valve electromagnetic coil insulation under thermal deterioration," in *Proc. 62nd IIS MFPT/ISA*, 2016, pp. 1386–1387.

[34] K. Wang, H. Guo, A. Xu, Z. Liu, C. Li, F. Kong, and S. Qi, "Degradation monitoring of low-voltage electromagnetic coil insulation based on microscopic image analysis," in *Proc. PHM*, Oct. 2018, pp. 692–696.

[35] M. Graves and G. Batchelor, *Machine Vision for the Inspection of Natural Products*. New York, NY, USA: Springer, 2003.

[36] J. Beyerer, F. P. León, and C. Frese, *Machine Vision: Automated Visual Inspection: Theory, Practice and Applications*. Berlin, Germany: Springer, 2016.

[37] C. Steger, M. Ulrich, and C. Wiedemann, *Machine Vision Algorithms and Applications*, 2nd ed. London, U.K.: Wiley, 2018.

[38] C. Li, K. Wang, and N. Xu, "A survey for the applications of content-based microscopic image analysis in microorganism classification domains," *Artif. Intell. Rev.*, vol. 51, no. 4, pp. 577–646, 2019.

[39] S. Chen, M. Zhao, G. Wu, C. Yao, and J. Zhang, "Recent advances in morphological cell image analysis," *Comput. Math. Methods Med.*, vol. 2012, Oct. 2011, Art. no. 101536.

[40] J. A. A. Jothi and V. M. A. Rajam, "A survey on automated cancer diagnosis from histopathology images," *Artif. Intell. Rev.*, vol. 48, no. 1, pp. 31–81, 2017.

[41] Z. Gácsi, "The application of digital image processing to materials science," *Mater. Sci. Forum*, vols. 414–415, pp. 213–220, Jan. 2003.

[42] C. Li, K. Shirahama, and M. Grzegorzek, "Environmental microbiology aided by content-based image analysis," *Pattern Anal. Appl.*, vol. 19, no. 2, pp. 531–547, 2016.

[43] J. Xu, X. Luo, G. Wang, H. Gilmore, and A. Madabhushi, "A deep convolutional neural network for segmenting and classifying epithelial and stromal regions in histopathological images," *Neurocomputing*, vol. 191, pp. 214–223, May 2016.

[44] C. Li, X. Huang, T. Jiang, and N. Xu, "Full-automatic computer aided system for stem cell clustering using content-based microscopic image analysis," *Biocybernetics Biomed. Eng.*, vol. 37, no. 3, pp. 540–558, 2017.

[45] N. Schlüter and F. Faul, "Matching the material of transparent objects: The role of background distortions," *i-Perception*, vol. 7, no. 5, pp. 1–24, 2016.

[46] G. Zhang, M. J. Pérez-Jiménez, and M. Gheorghe, *Real-Life Applications With Membrane Computing*. Cham, Switzerland: Springer, 2017.

[47] G. Zhang, J. Cheng, T. Wang, X. Wang, and J. Zhu, *Membrane Computing: Theory and Applications*. Beijing, China: Science Press, 2015.

[48] G. Păun, *Membrane Computing: An Introduction*. Berlin, Germany: Springer, 2002.

[49] G. Păun, G. Rozenberg, and A. Salomaa, *The Oxford Handbook of Membrane Computing*. London, U.K.: Oxford Univ. Press, 2010.

[50] M. Gheorghe, G. Păun, M. J. Pérez-Jiménez, and G. Rozenberg, "Frontiers of membrane computing: Open problems and research topics," *Int. J. Found. Comput. Sci.*, vol. 24, no. 5, pp. 547–624, 2013.

[51] G. Păun, "A quick introduction to membrane computing," *J. Logic Algebr. Program.*, vol. 79, no. 6, pp. 291–294, 2010.

[52] C. Buiu, C. Vasile, and O. Arsene, "Development of membrane controllers for mobile robots," *Inf. Sci.*, vol. 187, pp. 33–51, Mar. 2012.

[53] R. Yahya, S. Shamsuddin, S. I. Yahya, S. Hasan, B. Al-Salibi, and G. Al-Khafaji, "Image segmentation using membrane computing: A literature survey," in *Bio-Inspired Computing—Theories and Applications*, M. Gong, L. Pan, T. Song, and G. Zhang, Eds. Singapore: Springer, 2016, pp. 314–335.

[54] X. Wang, G. Zhang, F. Neri, T. Jiang, J. Zhao, M. Gheorghe, F. Ipate, and R. Lefticaru, "Design and implementation of membrane controllers for trajectory tracking of nonholonomic wheeled mobile robots," *Integr. Comput.-Aided Eng.*, vol. 23, no. 1, pp. 15–30, 2016.

[55] T. Wang, G. Zhang, and M. Pérez-Jiménez, "Fault diagnosis models for electric locomotive systems based on fuzzy reasoning spiking neural P systems," in *Membrane Computing* (Lecture Notes in Computer Science), vol. 8961, M. Gheorghe, G. Rozenberg, A. Salomaa, P. Sosík, and C. Zandron, Eds. Cham, Switzerland: Springer, 2014, pp. 385–395.

[56] D. Díaz-Pernil and A. Berciano, F. Peña-Cantillana, and M. A. Gutiérrez-Naranjo, "Segmenting images with gradient-based edge detection using membrane computing," *Pattern Recognit. Lett.*, vol. 34, no. 18, pp. 846–855, 2013.

[57] H. Peng, J. Wang, and M. Pérez-Jiménez, "Optimal multi-level thresholding with membrane computing," *Digit. Signal Process.*, vol. 7, pp. 53–64, Feb. 2015.

[58] D. Guo, G. Zhang, Y. Zhou, J. Yuan, P. Paul, K. Fu, and M. Zhu, "Image thresholding using a modified membrane-inspired algorithm based on particle swarm optimization with hyperparameter," in *Proc. ACMC*, 2018, pp. 318–340.

[59] T. M. Mitchell, *Machine Learning*. New York, NY, USA: McGraw-Hill, 1997.

[60] J. A. Hoeting, D. Madigan, A. E. Raftery, and C. T. Volinsky, "Bayesian model averaging: A tutorial," *Statist. Sci.*, vol. 14, no. 4, pp. 382–401, 1999.

[61] L. Breiman, "Bagging predictors," *Mach. Learn.*, vol. 24, no. 2, pp. 123–140, 1996.

[62] C. Li, *Content-based Microscopic Image Analysis*. Berlin, Germany: Logos Verlag Berlin GmbH 2016.

[63] X. He, R. Zemel, and M. A. Carreira-Perpinan, "Multiscale conditional random fields for image labeling," in *Proc. CVPR*, Jun./Jul. 2004, pp. II.

[64] I. Zyout, J. Czajkowska, and M. Grzegorzek, "Multi-scale textural feature extraction and particle swarm optimization based model selection for false positive reduction in mammography," *Comput. Med. Imag. Graphics*, vol. 46, no. 2, pp. 95–107, 2015.

[65] L. Deng and D. Yu, "Deep learning: Methods and applications," *Found. Trends Signal Process.*, vol. 7, nos. 3–4, pp. 1–199, 2014.

[66] Y. Bengio, "Learning deep architectures for AI," *Found. Trends Mach. Learn.*, vol. 2, no. 1, pp. 1–127, 2009.

[67] I. Hadji and R. P. Wildes, "What do we understand about convolutional networks?" 2018, *arXiv:1803.08834*. [Online]. Available: https://arxiv.org/abs/1803.08834

[68] S. Dieleman. (2015). *Classifying Plankton With Deep Neural Networks*. [Online]. Available: https://benanne.github.io/2015/03/17/plankton.html

[69] S. Kosov, K. Shirahama, C. Li, and M. Grzegorzek, "Environmental microorganism classification using conditional random fields and deep convolutional neural networks," *Pattern Recognit.*, vol. 77, pp. 248–261, May 2018.

[70] G. Guo and C. R. Dyer, "Learning from examples in the small sample case: Face expression recognition," *IEEE Trans. Syst., Man, Cybern., B, Cybern.*, vol. 35, no. 3, pp. 477–488, Jun. 2005.

[71] J. Deng, W. Dong, R. Socher, L.-J. Li, K. Li, and L. Fei-Fei, "ImageNet: A large-scale hierarchical image database," in *Proc. CVPR*, Jun. 2009, pp. 248–255.

[72] S. P. K. Karri, D. Chakraborty, and J. Chatterjee, "Transfer learning based classification of optical coherence tomography images with diabetic macular edema and dry age-related macular degeneration," *Biomed. Opt. Express*, vol. 8, no. 2, pp. 579–592, 2017.

[73] C. G. M. Snoek, M. Worring, and A. W. M. Smeulders, "Early versus late fusion in semantic video analysis," in *Proc. ACM ICMR*, 2005, pp. 399–402.

[74] H. Anton, *Elementary Linear Algebra*, 7th ed. Hoboken, NJ, USA: Wiley, 1994.

[75] G. Sidorov, A. Gelbukh, H. Gómez-Adorno, and D. Pinto, "Soft similarity and soft cosine measure: Similarity of features in vector space model," *Computación Sistemas*, vol. 18, no. 3, pp. 491–504, 2014.

[76] E. Levina and P. Bickel, "The earth mover's distance is the mallows distance: Some insights from statistics," in *Proc. ICCV*, Jul. 2001, pp. 251–256.

[77] J. Voit, *The Statistical Mechanics of Financial Markets*. Berlin, Germany: Springer-Verlag, 2003.

[78] R. Gonzalez and R. Woods, *Digital Image Processing*, 4th ed. London, U.K.: Pearson, 2017.

[79] B. Hüttenrauch, "Literature review on data augmentation," in *Targeting Using Augmented Data in Database Marketing*, B. Hüttenrauch and G. Krämer, Eds. Berlin, Germany: Springer, 2016, pp. 71–104.

[80] C. Poynton, *Digital Video and HDTV: Algorithms and Interfaces*. San Mateo, CA, USA: Morgan Kaufmann, 2003.

[81] M. K. Agoston, *Computer Graphics and Geometric Modelling*. London, U.K.: Springer, 2005.

[82] M. Ebner, *Color Constancy*. Hoboken, NJ, USA: Wiley, 2007.

[83] C. Poynton. (1999). *YUV and Luminance Considered Harmful*. [Online]. Available: http://poynton.ca/PDFs/YUV_and_luminance_harmful.pdf

[84] R. M. Haralick, K. Shanmugam, and I. Dinstein, "Textural features for image classification," *IEEE Trans. Syst., Man, Cybern.*, vol. SMC-3, no. 6, pp. 610–621, Nov. 1973.

[85] K. Pearson, "On lines and planes of closest fit to systems of points in space," *Philos. Mag.*, vol. 2, no. 6, pp. 559–572, 1901.

[86] S. Bochner and K. Chandrasekharan, *Fourier Transforms*. London, U.K.: Princeton Univ. Press, 1949.

[87] B. S. Manjunath and W. Y. Ma, "Texture features for browsing and retrieval of image data," *IEEE Trans. Pattern Anal. Mach. Intell.*, vol. 18, no. 8, pp. 837–842, Aug. 1996.

[88] N. Dalal and B. Triggs, "Histograms of oriented gradients for human detection," in *Proc. CVPR*, Jun. 2005, pp. 886–893.

[89] K. Simonyan and A. Zisserman, "Very deep convolutional networks for large-scale image recognition," 2014, *arXiv:1409.1556*. [Online]. Available: https://arxiv.org/abs/1409.1556

[90] R. Palmer, "Polyamides, plastics," in *Encyclopedia of Polymer Science and Technology*. New York, NY, USA: Wiley, 2001.

[91] R. I. Stephens, A. Fatemi, R. R. Stephens, and H. Fuchs, *Metal Fatigue in Engineering*, 2nd ed. Hoboken, NJ, USA: Wiley, 2001.

[92] J. C. Lim and T. Ozbakkaloglu, "Influence of concrete age on stress–strain behavior of FRP-confined normal- and high-strength concrete," *Construct. Building Mater.*, vol. 82, no. 4, pp. 61–70, 2015.

[93] I. J. Goodfellow, J. Pouget-Abadie, M. Mirza, B. Xu, D. Warde-Farley, S. Ozair, A. Courville, and Y. Bengio, "Generative adversarial networks," 2014, *arXiv:1406.2661*. [Online]. Available: https://arxiv.org/abs/1406.2661

[94] C. Li and M. Wand, "Combining Markov random fields and convolutional neural networks for image synthesis," in *Proc. CVPR*, Jun. 2016, pp. 2479–2486.

[95] J. Cheng, G. Zhang, F. Caraffini, and F. Neri, "Multicriteria adaptive differential evolution for global numerical optimization," *Integr. Comput.-Aided Eng.*, vol. 22, no. 2, pp. 103–117, 2015.

[96] B. Xu, P. Guo, and C. L. P. Chen, "An adaptive regularization method for sparse representation," *Integr. Comput.-Aided Eng.*, vol. 21, no. 1, pp. 91–100, 2014.

[97] S. Wu, G. Zhang, M. Zhu, T. Jiang, and F. Neri, "Geometry based three-dimensional image processing method for electronic cluster eye," *Integr. Comput.-Aided Eng.*, vol. 25, no. 3, pp. 213–228, 2018.

[98] F. Fernández-Luque, D. Pérez, J. Zapata, and R. Ruiz, "Automatically calibrated occupancy sensors for an ambient assisted living system," *Integr. Comput.-Aided Eng.*, vol. 23, no. 3, pp. 287–298, 2016.

[99] T. Ho, "Random decision forests," in *Proc. ICDAR*, Aug. 1995, pp. 278–282.

CHEN LI received the B.E. degree from the University of Science and Technology Beijing, China, in 2008, the M.Sc. degree from Northeast Normal University, China, in 2011, and the Dr.-Ing. degree from the University of Siegen, Germany, in 2016. From 2016 to 2017, he was a Postdoctoral Researcher with the Johannes Gutenberg University of Mainz, Germany. He is currently an Associate Professor with Northeastern University. He is also the Head of the Research Group for Microscopic Image and Medical Image Analysis, Northeastern University. His research interests include microscopic image analysis, medical image analysis, machine learning, pattern recognition, machine vision, multimedia retrieval, and membrane computing.

FANJIE KONG received the B.E. degree from the Research Group for Microscopic Image and Medical Image Analysis, Northeastern University, China, in 2018. He is currently pursuing the master's degree with Duke University, USA. His research interest includes image analysis, machine learning, and membrane computing.

KAI WANG received the Ph.D. degree in mechatronic engineering from the Shenyang Institute of Automation (SIA), Chinese Academy of Sciences (CAS). He was a Visiting Scholar with the Center for Advanced Life Cycle Engineering (CALCE), University of Maryland, from 2014 to 2016. He is currently an Associate Professor with SIA, CAS. He is also a Tutor for graduate students with the University of CAS. His primary research interests include fault diagnosis, prognostics and health management, and reliability engineering. Recently, he is specially focused on degradation mechanisms of electromagnetic coil insulation and methods to detect degraded insulation prior to the formation of shorts in electromagnetic coils. He received the Best Academic Presentation Award at the 2013 IEEE International Conference on Electronic Measurement & Instruments.

AIDONG XU was born in Liaoning, China, in 1969. He received the Ph.D. degree from Shenyang Institute of Automation (SIA), Chinese Academy of Sciences, in 2012, where he is currently a Research Fellow. His research interests include industrial digital communications, functional security technologies, and fault diagnosis. He is a member of the fourth Technical Committee (Field bus) of the National Industrial Process Measurement and Control Standardization Technical Committee and an expert at the International Electro Technical Commission/Industrial Process Measurement and Control Committee/Digital Communications Subcommittee/Real-Time Ethernet Working Group (IEC/SC65C/WG11).
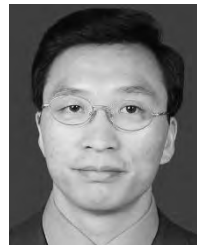
GEXIANG ZHANG was born in 1974. He was a Visiting Researcher with the Research Group of Prof. Marian Gheorghe, University of Sheffield, U.K., the Research Group of Prof. Mario J. Perez-Jimenez, University of Seville, Spain, and the Research Group of Prof. Nadrian C. Seeman, New York University, USA. He is currently a Professor with the Southwest Jiaotong University, China. He is also a Guest Professor with Xihua University, China. He has published three books and more than 30 papers about membrane in high level journals and conferences. His research interests include membrane computing, evolutionary computation, smart power grids, and robot control. He is also the Chairman of the Chinese Membrane Commuting Society.

NING XU received the bachelor's degree from Shenyang University, China, in 2008, the master's degree from the Northeast Normal University, China, in 2011, and the Ph.D. degree from the University of Siegen, Germany, in 2016. Since 2017, she has been a Lecturer with Liaoning Shihua University, China. Her research interests include image and video analysis.

ZHIHUA LIU was born in Liaoning, China, in 1977. He received the Ph.D. degree in pattern recognition and intelligent systems from the Shenyang Institute of Automation (SIA), Chinese Academy of Sciences (CAS), in 2008, where he is currently an Associate Professor. His primary research interests include nanomanipulation methods, nanoscale measurement, and image processing method at micro/nano scale.

HAIFENG GUO was born in Liaoning, China, in 1979. He received the degree from Northeastern University, China, in 2009. He is currently pursuing the Ph.D. degree with the Shenyang Institute of Automation, University of Chinese Academy of Sciences. His research interests include degradation mechanisms of transformer winding insulation and methods to detect degraded insulation prior to the formation of shorts in windings, fault prediction and health management, and reliability engineering.

XUE WANG received the bachelor's and master's degrees from Northeastern University, China, in 2014 and 2017, respectively, where she is currently an Engineer. Her research interest includes machine design.

KUAN LIANG received the bachelor's degree from Northeastern University, China, in 2014, where he is currently an Engineer with the Research Group for Microscopic Image and Medical Image Analysis. His research interest includes machine design.

JIANYING YUAN received the B.S. degree in biomedical engineering and the master's degree in pattern recognition and intelligent system from Southwest University of Science and Technology, China, in 2005 and 2008, respectively, and the Ph.D. degree in mechanical design and theory from Southwest Jiao Tong University, China, in 2015. She is currently a Lecturer with the Chengdu University of Information Technology, China, meanwhile, she is also a Postdoctoral Researcher with the University of Electronic Science and Technology, China. Her research interests include computer vision and membrane computing. Till now, she has published three papers about membrane computing.

SHOULIANG QI received the Ph.D. degree from Shanghai Jiaotong University, in 2007. He joined the GE Global Research Center. From 2014 to 2015, he was a Visiting Scholar with the Eindhoven University of Technology and the Epilepsy Center Kempenhaeghe, The Netherlands. He is currently an Associate Professor with the Northeastern University, China. In recent years, he has been conducting productive studies in the intelligent medical imaging computing and modeling, machine learning, brain networks, and brain models. He has published over 80 papers in peer-reviewed journals and international conferences. He has received academic awards such as the Chinese Excellent Ph.D. Dissertation Nomination Award.

TAO JIANG was born in 1975. He received the Ph.D. degree from the University of Siegen, Germany, in 2013. He is currently a Professor with the Chengdu University of Information Technology (CUIT), China. He is also the Dean with the Control Engineering College of CUIT. His research interests include machine vision, artificial intelligence, robot control, self-driving auto, and membrane computing.

• • •